Title: The molecular infrastructure of glutamatergic synapses in the mammalian forebrain

Authors:

J. Peukes[1,2], C. Lovatt[3,4], C. Leistner[3,5], J. Boulanger[1], D. R. Morado[1,6], M. J. G. Fuller[3], W. Kukulski[1,7], F. Zhu[8], N. H. Komiyama[8,9], J. A. G. Briggs[1,10], S. G. N. Grant[8], R. Frank[1,3*]

Affiliations:

[1] MRC Laboratory of Molecular Biology, Francis Crick Avenue, Cambridge, CB2 0QH, UK.

[2] Current address: University of California Berkeley, QB3, Berkeley, USA

[3] Astbury Centre for Structural Molecular Biology, School of Biomedical Sciences, Faculty of Biological Sciences, University of Leeds, LS2 9JT, UK.

[4] Current address: Rosalind Franklin Institute, Didcot, OX11 0QS, UK.

[5] Current address: Harvard Medical School

[6] Current address: Science for Life Laboratory, Department of Biochemistry and Biophysics, Stockholm University, 17165 Solna, Sweden.

[7] Current address: Institute of Biochemistry and Molecular Medicine, University of Bern, 3012 Bern, Switzerland.

[8] Genes to Cognition Program, Centre for Clinical Brain Sciences, Simons Initiative for the Developing Brain, University of Edinburgh, Edinburgh EH16 4SB, UK.

[9] Genes to Cognition Program, Centre for Clinical Brain Sciences, Simons Initiative for the Developing Brain, the Muir Maxwell Epilepsy Centre, University of Edinburgh, Edinburgh EH16 4SB, UK.

[10] Max Planck Institute of Biochemistry, Martinsried, Germany.

* Corresponding author. Email: r.frank@leeds.ac.uk

Abstract

Glutamatergic synapses form the vast majority of connections within neuronal circuits, but how these subcellular structures are molecularly organized within the mammalian brain is poorly understood. Conventional electron microscopy using chemically fixed, metal-stained tissue has identified a proteinaceous, membrane-associated thickening called the 'postsynaptic density' (PSD). Here, we combined mouse genetics and cryo-electron tomography to determine the 3D molecular architecture of fresh isolated and anatomically intact synapses in the adult forebrain. The native glutamatergic synapse did not consistently show a high density of proteins at the postsynaptic membrane thought to be characteristic of the PSD. Instead, a 'synaptoplasm' consisting of cytoskeletal elements, macromolecular complexes and membrane-bound organelles extended throughout the pre- and post-synaptic compartments. Snapshots of active processes gave insights into membrane remodeling processes. Clusters of 4-60 ionotropic glutamate receptors were positioned inside and outside the synaptic cleft. Together, these information-rich tomographic maps present a detailed molecular framework for the coordinated activity of synapses in the adult mammalian brain.

INTRODUCTION

Glutamate is the major chemical neurotransmitter in the mammalian brain that mediates communication within neuronal circuits at specialized cell-cell junctions called synapses. The molecular composition of glutamatergic synapses is highly complex, reflecting the many different molecular machines required to subserve diverse synaptic functions, including learning and memory (Chua et al., 2010; Ebrahimi and Okabe, 2014; Frank et al., 2016; Nakahata and Yasuda, 2018). Indeed, more than a thousand different synaptic proteins have been identified in the mouse and human forebrain (Bayés et al., 2011; Roy et al., 2017). How this ensemble of macromolecules is structurally organized within mammalian brain synapses is currently unknown.

Cryo-electron microscopy (cryoEM) has the potential to reveal the native 3-dimensional molecular architecture of mammalian brain synapses but with the limitation that samples must be vitreous and less than ~300 nm thick. Although primary neurons grown on EM grids can overcome this constraint (Asano et al., 2015; Tao et al., 2018), the environment in which *in vitro* cultured cells grow differs markedly from tissues. Indeed, primary neurons *in vitro* appear unable to reach the molecular and functional maturity of neurons from the brain itself (Frank et al., 2016; Harris and Pettit, 2007). While brain synapses can be isolated by biochemical fractionation (Whittaker, 1959), these enrichment steps delay cryopreservation by at least an hour and involve non-physiological buffers that together cause deterioration of certain macromolecular structures. An example is the cytoskeleton, particularly microtubules, which rapidly depolymerize within a matter of 1-3 minutes if the provision of nucleotide triphosphates or cellular integrity becomes compromised (Mitchison, 1995; Pollard and Mooseker, 1981).

To minimize deterioration of tissue samples we developed an 'ultra-fresh' sample preparation workflow without fractionation by combining mouse genetic labelling of synapses (Zhu et al., 2018) with cryogenic correlated light and electron microscopy (cryoCLEM) and cryo-electron tomography (cryoET) (**Figure 1A**). Guided by the mouse genetic fluorescent label in our cryoCLEM workflow, we also determined the in-tissue 3D structure of synapses from cryo-sections of mouse cortex and hippocampus. These

ultra-fresh and in-tissue structural data indicate that the near-physiological molecular architecture of glutamatergic synapses was highly variable in composition, copy number and distribution of organelles and macromolecular assemblies. The molecular density of protein complexes in the postsynaptic cytoplasm was variable and did not indicate a conserved higher density of proteins at the postsynaptic membrane corresponding to a postsynaptic density (PSD).

RESULTS

CryoCLEM of adult brain glutamatergic synapses

To determine the molecular architecture of adult forebrain excitatory synapses, we used knockin mice, in which the gene encoding PSD95 was engineered to include an in-frame, C-terminal fusion of the fluorescent tag, EGFP (*Psd95*$^{GFP/GFP}$) (Broadhead et al., 2016; Frank et al., 2016; Zhu et al., 2018). PSD95 is a membrane-associated cytoplasmic protein that concentrates exclusively within mature glutamatergic synapses (Chen et al., 2000; El-Husseini et al., 2000) and forms supercomplexes with ionotropic glutamate receptors that reside in the postsynaptic membrane (Frank et al., 2016). Fresh *Psd95*$^{GFP/GFP}$ mouse forebrains, encompassing cortex and hippocampus, were homogenized in ice-cold ACSF, then immediately vitrified on EM grids. Sample preparation was completed within 2 minutes, the time taken to cull the mouse, dissect and homogenize the forebrain, and plunge-freeze the sample on a blotted cryoEM grid (**Figure 1A**).

The GFP signal from *Psd95*$^{GFP/GFP}$ knockin mice pinpoints the location of mature glutamatergic synapses without over-expression or any detectible effect on synapse function (Broadhead et al., 2016). Thus, cryoEM grids were imaged on a cryogenic fluorescence microscope (cryoFM) revealing PSD95-GFP puncta (**Figure 1A**), absent in WT control samples (**Figure 1–figure supplement 1A**), which resembled those observed by confocal fluorescent imaging of the brain (Zhu et al., 2018). Using a cryoCLEM workflow, the same grids were then imaged by cryoEM and fluorescent PSD95-GFP puncta were mapped onto the cryoEM image (**Figure 1B**). These cryoCLEM images

showed PSD95-GFP puncta that were invariably associated with membrane-bound subcellular compartments (100 to 1,300 nm diameter) (**Figure 1B**).

To resolve the molecular architecture within PSD95-containing puncta, we acquired 93 PSD95-GFP cryoCLEM-guided cryo-electron tomographic tilt series from 5 adult mouse forebrains. Aligned tilt series were reconstructed to produce 3-dimensional tomographic maps as shown in **Figure 1C** and D (see also **Figure 1–table 1** and **Figure 1–video 1-7** showing representative tomographic volumes of ultra-fresh synapses; all tomograms available in the EMPIAR database upon publication). As expected, all GFP-positive membranes were attached to a neighbouring membrane, of which 78% were closed compartments and enriched in synaptic vesicles that characterize the presynaptic compartment. All but three of the presynaptic compartments (96%) contained docked synaptic vesicles tethered 2-8 nm from presynaptic membrane (**Figure 1–figure supplement 1B**). Thus, our PSD95-GFP cryoCLEM workflow enabled identification of the pre- and post-synaptic membrane of glutamatergic synapses (hereon referred to as PreSM and PoSM, respectively).

The high quality of the tomographic maps enabled assignment of cytoskeletal elements within the synapse, including extensive networks of filamentous actin (F-actin). These were identifiable with a diameter of 7 nm and apparent helical arrangement of subunits (Hanson, 1967) in all PoSM compartments (Okamoto et al., 2007) (**Figure 1C-E** and **Figure 1–figure supplement 1C**) and in 49±7% (mean ± SEM, n=5 mice) of PreSM compartments (**Figure 1E** and **Figure 1–figure supplement 1D**). In PreSM that lacked an apparent F-actin cytoskeletal network, we cannot exclude the possibility that actin is present in monomeric form or very short actin filaments, which cannot be unambiguously identified in our tomograms. Microtubules were identified (25 nm diameter) in 15±2% of PreSM (**Figure 1C**, **D**, and **F**), but as expected were absent from the PoSM. Notwithstanding the mechanical stress of detaching synaptic terminals to cryopreserve whole synapses, this extensive actin and microtubular cytoskeleton corroborates the maintenance of macromolecular structures near to their physiological context.

Molecular crowding within the synapse

We first assessed the overall architecture of macromolecules within the synapse by measuring macromolecular crowding (Smith and Langmore, 1992) (see methods and **Figure 1–figure supplement 2** detailing how molecular density was measured and how errors can arise). Based on conventional EM experiments of fixed, dehydrated, heavy-metal-stained tissue, glutamatergic synapses are marked by the presence of a 30-50 nm layer of densely packed proteins opposite the active zone on the cytoplasmic side of the PoSM, called the postsynaptic density (PSD) that defines every glutamatergic synapse (Bourne and M.Harris, 2008; Gray, 1959; Sheng and Kim, 2011). However, within fresh, adult brain synapse structures reported here this region of higher density at the postsynaptic membrane was not a conserved feature of all PSD95-GFP-containing glutamatergic synapses (**Figure 1g** and see also the central density profiles of each synapse in **Figure 1–figure supplement 3**). The distribution of molecular densities was variable with half the population of synapses showing a significant relative increase in molecular density in proximal versus distal regions (5-30 nm versus 50-200 nm from the PoSM) of cytoplasm in the postsynaptic compartment (**Figure 1H**). The remaining subpopulations of synapses did not have a higher density or contained a significantly lower relative molecular density at regions proximal to the PoSM (**Figure 1H**). These data suggest that a higher density of proteins characteristic of the PSD is not a conserved feature with adult mouse brain glutamatergic synapses (Tao et al., 2018).

To examine further molecular crowding within anatomically intact postsynaptic compartments, fresh, acute brain tissues of adult *Psd95*$^{GFP/GFP}$ mice were cryopreserved by high-pressure freezing. Next, 70-150 nm thin, vitreous sections of the cortex and hippocampus were collected by cryo-ultramicrotomy (**Figure 2A**) (Zuber et al., 2005). Glutamatergic synapses were identified by cryoCLEM (**Figure 2B**) and cryo-electron tomograms were collected revealing the native in-tissue 3D architecture of glutamatergic synapses (**Figure 2C-D** and **Figure 2–figure supplement 1A** and **Figure 2-video 1-2**). The PoSM was identified by cryoCLEM and the PreSM by the presence of numerous synaptic vesicles. These in-tissue 3D tomographic maps also resolved individual cytoskeletal elements, membrane proteins, and numerous other subcellular structures that were consistent with those observed in ultra-fresh synapse cryoET data (**Figure 2–table**

1).

Molecular density profiles of in-tissue synapse cryoET data showed that the density of proteins in the cytoplasm proximal to the PoSM relative to distal regions was highly variable (**Figure 2E** and see also profiles of each synapse in **Figure 2–figure supplement 1B**). Less than half the population of synapses contained a significant relative increase in molecular density in regions of the cytoplasm proximal to the PoSM (5-30 nm versus 50-200 nm from the PoSM, **Figure 2F**). The remaining subpopulations of synapses lacked a higher density or contained a significantly lower relative molecular density at regions proximal to the PoSM (**Figure 2F**). No significant difference was observed comparing synapses from the cortex versus hippocampus, as expected (Zhu et al., 2018). The variability of molecular crowding in these near-physiological in-tissue synapses were consistent with the ultra-fresh synapse tomograms, indicating that the presence of even a slight increase in cytoplasmic molecular density that could correspond to a PSD was not a conserved feature of glutamatergic synapses.

To rule out that the absence of a conserved postsynaptic protein dense region was caused by the *Psd95*$^{GFP/GFP}$ knock-in mutation or the method of sample preparation, we performed conventional EM of acute slice brain samples and ultra-fresh synapses, which both showed a PSD in samples from *Psd95*$^{GFP/GFP}$ comparable to those in wildtype mice (**Figure 2G-H** and **Figure 2–figure supplement 2A-B**). This confirmed that the appearance of the high local protein density that defines the PSD is a consequence of conventional EM sample preparation methods.

Synaptic organelles

To assess the molecular diversity of adult forebrain excitatory synapse architecture we next catalogued the identifiable macromolecular and organelle constituents in ultra-fresh synapses (**Figure 1–table 1**). At least one membrane-bound organelle was present in 61±4% of PoSM compartments and, excluding synaptic vesicles, in 77±2% of PreSM compartments (**Figure 3–figure supplement 1A**). Based on previous characterizations by conventional EM studies (Cooney et al., 2002) most membrane-bound organelles were

readily separable into three structural classes (**Figure 3–figure supplement 1B** and **Figure 1–table 1**, see methods): 1) A network of flat, tubular membrane compartments that twisted and projected deep toward the adhered synaptic membrane (**Figure 3A** and **Figure 3–figure supplement 1B-C**). 2) Large spheroidal membrane compartments (>60 nm diameter) that were situated 72-500 nm away from the cleft (**Figure 3A** and **Figure 3–figure supplement 1B**, **D**). 3) Multivesicular bodies that were positioned throughout the PreSM and PoSM (78-360 nm away from the cleft, **Figure 3B** and **Figure 3–figure supplement 1B**, **E**). A fourth category of membranous compartments found in our data did not match any of the structures previously reported and can be characterized as polyhedral vesicles with flat surfaces and joined by protein-coated membrane edges and vertices (90° to 35° internal angle, **Figure 3C** and **Figure 3–figure supplement 1F**). Except for mitochondrial cristae, internal membranes with this high curvature have not been reported in non-neuronal cells (Bykov et al., 2017; Engel et al., 2015).

Mitochondria were also readily identified, most abundantly in the presynaptic compartment (44±5% of PreSM) and only once in close proximity to the postsynaptic compartment (**Figure 3–figure supplement 1G**). A striking feature of all presynaptic mitochondria was the presence of amorphous dense aggregates within the mitochondrial matrix (**Figure 3–figure supplement 1H**). Similar aggregates have been identified as solid deposits of calcium phosphate (Wolf et al., 2017) and are apparent in cultured cells (Tao et al., 2018). To exclude the possibility that mitochondrial aggregates arose by excitation during sample preparation we collected tomograms of ultra-fresh synapses prepared in ACSF that lacked divalent cations, including calcium (**Figure 3–figure supplement 1I**). These data showed synapses with mitochondrial aggregates in the absence of exogenous calcium, suggesting they do not arise during sample preparation. Thus, mitochondrial granular aggregates likely represent a physiologically normal feature of the mammalian brain, which is in keeping with the role of synaptic mitochondria as a reservoir of cellular calcium ions (Billups and Forsythe, 2002). Overall, the variable protein composition and type of intracellular organelles indicate distinct synapse subtypes or states within the mammalian forebrain.

Synaptic shape and remodeling

Further diversity of synaptic architectures was evident in the size, shape and mode of connectivity of the PreSM to the PoSM (Zhu et al., 2018). To assess these structural variables, PSD95-GFP-containing PoSMs and apposing PreSMs were semi-automatically segmented (see methods). This revealed synapses with multiple different topologies, including with a single, double, and divergent (1 PreSM: 2 PoSM) synaptic contacts (**Figure 3D**, *top*, *middle* and *bottom*, respectively and **Figure 1–table 1**). These were consistent with the known diversity of cellular connectivity mediated by glutamatergic synapses (Harris and Weinberg, 2012). The volume of the PoSM compartment in our dataset ranged from $3x10^6$ to $79x10^6$ nm^3. In keeping with the known diversity of PSD95-containing synapses (Zhu et al., 2018), PoSM size was not correlated with the amount of PSD95-GFP detected by cryoCLEM (P=0.7, Pearson's r=0.06, **Figure 3E**), which is consistent with *in vivo* fluorescence experiments (Melander et al., 2021). However, PoSM size was correlated with the number of actin cytoskeletal filaments (P<0.0001, Pearson's r=0.83, **Figure 3F**), which is in line with the apparent non-uniform distribution of F-actin in distinct sub-cellular compartments (**Figure 1E**) and the role of F-actin in regulating postsynaptic geometry and structural plasticity (Okamoto et al., 2007).

The variation in size, shape and molecular composition of synaptic membranes is thought to arise by membrane remodeling, including exo- and endocytosis. In 32±6% synapses we identified pit-like, hemifusion or hemifission structures in the membrane (**Figure 3–figure supplement 1J**) that likely indicate intermediates of membrane remodeling trapped within the sample at the moment of freezing (**Figure 1–table 1**). Significantly more remodeling intermediates were identified in the PreSM compared to PoSM compartments (**Figure 3G**), which is consistent with the expected high frequency of membrane dynamics associated with synaptic vesicle recycling in this compartment (Kononenko and Haucke, 2015).

In a subset of tomograms (21±11%, Fig 3h) a clathrin coat was unambiguously identified by the triskelion-forming pentagonal and hexagonal openings (Kanaseki and Kadota, 1969) evident in the raw tomographic maps (**Figure 1–table 1**). In the pre-synaptic compartment, clathrin surrounded synaptic vesicles (**Figure 3I**) and budding vesicles on internal membrane compartments (**Figure 3J**), which is in agreement with previous time-

resolved EM experiments (Watanabe et al., 2014). In the postsynaptic compartment, a clathrin-coated pit formed directly on the cleft, suggesting membrane and cargo can be removed without prior lateral diffusion out of the synapse (**Figure 3K**). Thus, the distribution of these distinct intermediates suggests that membrane remodeling occurs at particular sub-compartments of the synapse (Borges-Merjane et al., 2020; Imig et al., 2020; Watanabe et al., 2014).

Synaptic cleft and ionotropic glutamate receptors

Geometric properties of each synapse are thought to be critical for determining synaptic strength, including synaptic cleft height (Cathala et al., 2005; Rusakov et al., 2011), measured as the shortest distance between PreSM and PoSM. To quantify this variable in our dataset we computationally determined the 3D coordinates of the cleft within each synapse (**Figure 4–figure supplement 1A** and see methods). The PreSM to PoSM distances across the cleft indicated an average cleft height of 33 nm (**Figure 4A**). These values differ from average cleft heights of ~20 nm determined in non-native conditions by conventional EM(Peters et al., 1970) but are consistent with super-resolution light microscopy imaging (Tønnesen et al., 2018). Interestingly, the average cleft height of each synapse in our dataset varied (ranging from 27 to 37 nm)[8]. A similar range of cleft distances were observed in in-tissue synapse tomograms (**Figure 2C** and **Figure 2–figure supplement 1**), suggesting that the cleft dimensions were largely unaffected by the ultra-fresh sample preparation. A subset of 'ultra-fresh' synapses maintained a very broad or bimodal distribution of cleft heights (**Figure 4–figure supplement 1B**). Inspection of synapses with a broad or bimodal distribution revealed closely apposed and remotely spaced subsynaptic regions of the cleft, containing transsynaptic complexes with varying dimensions that complemented the cleft height of the subregion (**Figure 4–figure supplement 1C-D**). Closely opposed synaptic subregions were found both near the edge and the middle of the cleft, consistent with the notion that cleft height is locally regulated. Thus, these data suggest the synaptic cleft as a highly plastic interface, in which cleft dimensions are dictated by the variable molecular composition of transsynaptic adhesion complexes (Missler et al., 2012).

The number, concentration, and distribution of ionotropic glutamate receptors anchored at the postsynaptic membrane by PSD95 is a central determinant of synaptic output (Béïque et al., 2006; Cathala et al., 2005; Kerr and Blanpied, 2012; Migaud et al., 1998; Rusakov et al., 2011; Tang et al., 2016). Putative ionotropic glutamate receptors were readily identified in 95±2% of PoSMs. These resembled the side (**Figure 4B** *left*) and top views (**Figure 4B** *right*) of ionotropic glutamate receptor atomic models (Hansen et al., 2021; Regan et al., 2015; Zhu and Gouaux, 2017). To confirm the identity of these proteins, we manually picked 2,522 receptors and extracted sub-volumes at those positions. We then applied subtomogram averaging procedures (see methods), which gave a 25 Å resolution 'Y' shaped cryoEM density map extending 14 nm from the PoSM (**Figure 4–figure supplement 2A**). The density shows a 2-fold symmetric structure containing two layers of globular domains in positions proximal and distal to the PoSM (**Figure 4C**) as expected for the structure of an ionotropic glutamate receptor. Consequently, the atomic structure of the AMPA receptor (Sobolevsky et al., 2009) was well accommodated by the density, which validates the identification of these ion channels within our synapse tomogram dataset (**Figure 4C**).

Next, to analyse the 3D configuration of populations of ionotropic glutamate receptors, we used these coordinates to quantify receptor clusters (see methods). Clusters were identified in 78% of synapses with an average of 2 clusters per synapse (**Figure 4D**), which were composed of 4 to 60 ionotropic glutamate receptors (average 10 receptors per cluster) (**Figure 4E**). These subsynaptic regions with higher concentrations of ionotropic glutamate receptors were reminiscent of receptor 'nanodomains' detected by super-resolution microscopy (Broadhead et al., 2016; Dani et al., 2010; MacGillavry et al., 2013; Nair et al., 2013; Tang et al., 2016).

The position of Ionotropic receptor clusters in synaptic and extra-synaptic sites, particularly the most abundant AMPA receptor subtype, is expected to impact synaptic strength and play an important role in synaptic plasticity (Park, 2018). We therefore analyzed the distribution of clusters in the context of the overall synapse architecture, which revealed that 60% of synapses maintained multiple large clusters of ionotropic glutamate receptors completely or partly outside of the cleft (**Figure 4D-F**). The

apparent detection of perisynaptic populations of glutamate receptors resemble the distributions observed by previous freeze-fracture immunogold EM (Masugi-Tokita and Shigemoto, 2007) and super-resolution light microscopy (Nair et al., 2013). The close proximity of perisynaptic clusters to the cleft is consistent with the functional necessity of a non-cleft population of ionotropic glutamate receptors that are recruited into the cleft during the early phase of long-term potentiation (Penn et al., 2017). Interestingly, the cytoplasmic C-termini of ionotropic receptor clusters both inside and outside of the cleft were associated with an elaborate and heterogeneous membrane- and actin-associated machinery (**Figure 4–figure supplement 2B**), possibly indicating that a structural mechanism contributes to the positioning of receptors both inside and outside the synaptic cleft.

Discussion

Here we determined the near-physiological 3D molecular architecture of glutamatergic synapses in the adult mammalian brain. In both ultra fresh and anatomically intact in-tissue cryoET datasets, a conserved relatively higher molecular density consistent with a PSD was absent. Instead, we observed subtle variations in molecular crowding within our cryoET dataset. The PSD has been a defining structure of glutamatergic synapses and has been most frequently observed by conventional EM (Bourne and M.Harris, 2008; Sheng and Kim, 2011), including when using more recent methods that involve freeze-substitution into organic solvents, followed by heavy-metal staining (Chen et al., 2008). We addressed the hypothesis that the occurrence of a PSD might be related to sample preparation and staining techniques of conventional EM by preparing the same mouse brain samples for conventional EM and were indeed able to reproduce the conserved occurrence of a PSD. We therefore suggest that the appearance of a PSD in room temperature EM experiments could arise during sample preparation. Preferential heavy-metal staining, crosslinking of interacting proteins by fixatives, or extraction of cytoplasmic proteins that are not directly or indirectly associated with the postsynaptic membrane could alter the apparent local distribution or relative density of proteins in tissue samples.

CryoEM of *in vitro* cultured organotypic slice cultures that first demonstrated the use of high-pressure freezing neuronal tissue samples, revealed synapses with various pre- and post- and trans-synaptic regions containing relatively higher densities (Zuber et al., 2005), albeit these data also lacked a label to confirm which synapses in the sample were glutamatergic.

Pioneering cryoET work of synapses purified from brain (synaptosomes) suggested a slightly higher relative molecular density juxtaposed to the postsynaptic membrane[56]. However, interpretation of synaptosome architectures may be compromised by lengthy sample preparation in non-physiological solutions that may cause a loss of cytoplasm and the native molecular architecture. Indeed, the marked absence of microtubules in synaptosomes is indicative of sample deterioration. It was also previously challenging to identify glutamatergic synapses definitively. Consequently, synaptosomes that lacked an apparent postsynaptic thickening were actively excluded from data collection (Martinez-Sanchez et al., 2021).

More recent cryoCLEM and cryoET studies of primary neuronal cell cultures identified glutamatergic synapses with some but not all showing a subtly higher concentration of macromolecules juxtaposed to the PoSM relative to distal regions deep within the postsynaptic compartment (Tao et al., 2018). These data were consistent with ultra-fresh synapse tomograms from adult brain, including the preservation of microtubules in the presynaptic compartment. A greater fraction of ultra-fresh adult synapses resembled the minority of primary neuronal synapses that lacked a relative increase in molecular crowding at the PoSM. In anatomically intact brain slice preparations that were nearer to physiological state of adult brain, even fewer instances of synapses were observed with a relative increase in molecular crowding of the cytoplasm at the PoSM. We suggest that these subtle differences of molecular crowding are likely a consequence of synapse heterogeneity (Zhu et al., 2018) or the source, in vitro cell culture versus adult brain, of central synapses. More broadly these cryoET data were consistent in suggesting that a relatively higher concentration of proteins juxtaposed to the PoSM is neither conserved nor a defining feature of glutamatergic synapses.

The synaptic architectures reported here were nevertheless consistent with the existence of specialized protein nanodomains of particular synaptic constituents detected by fluorescence labeling, including of PSD95 (Broadhead et al., 2016; Dani et al., 2010; MacGillavry et al., 2013; Nair et al., 2013; Tang et al., 2016). Indeed, clusters of ionotropic glutamate receptors that are anchored via interactions with PSD95 (Dani et al., 2010; MacGillavry et al., 2013; Nair et al., 2013; Tang et al., 2016) were a salient feature in tomographic maps of adult brain synapses.

We also evaluated the dimensions of the synaptic cleft, which is expected to affect synaptic strength (Rusakov et al., 2011). Cleft height was highly variable and on average 65% greater than that observed by conventional EM, which is also likely explained by the harsh treatments and the well-characterised shrinkage associated with chemical fixation of tissues in conventional EM. More broadly, these comparisons highlight the advantages of combining recent advances in cryoET (Turk and Baumeister, 2020) with genetic knockin labelling to determine the molecular architecture of fresh tissues.

Notwithstanding the absence of a conserved PSD, the arrangement of prominent constituents, including branched F-actin networks, organelles, ionotropic glutamate receptors and transsynaptic adhesion complexes, appeared to define the architecture of each glutamatergic synapse. Overall, the apparent variability of molecular and membrane architectures, from one synapse tomogram to the next, is in keeping with the enormous diversity of glutamatergic synapse types in the mammalian brain (Zhu et al., 2018). A future challenge will be to decipher how synaptic structural variability across the dendritic tree, different brain regions and neuronal subtypes determine specific functions within the mammalian brain.

References

Asano S, Fukuda Y, Beck F, Aufderheide A, Förster F, Danev R, Baumeister W. 2015. A molecular census of 26*S* proteasomes in intact neurons. *Science* **347**:439–442. doi:10.1126/science.1261197

Bayés A, Lagemaat LN van de, Collins MO, Croning MDR, Whittle IR, Choudhary JS, Grant SGN. 2011. Characterization of the proteome, diseases and evolution of the human postsynaptic density. *Nature Neuroscience* **14**:19–21.

Béïque J-C, Lin D-T, Kang M-G, Aizawa H, Takamiya K, Huganir RL. 2006. Synapse-specific regulation of AMPA receptor function by PSD-95. *Proc National Acad Sci* **103**:19535–19540. doi:10.1073/pnas.0608492103

Billups B, Forsythe ID. 2002. Presynaptic mitochondrial calcium sequestration influences transmission at mammalian central synapses. *Journal of Neuroscience* **22**:5840–5847.

Borges-Merjane C, Kim O, Jonas P. 2020. Functional Electron Microscopy, "Flash and Freeze," of Identified Cortical Synapses in Acute Brain Slices. *Neuron* **105**:992-1006.e6.

Bourne JN, M.Harris K. 2008. Balancing Structure and Function at Hippocampal Dendritic Spines. *Annu Rev Neurosci* **31**:47–67. doi:10.1146/annurev.neuro.31.060407.125646

Broadhead MJ, Horrocks MH, Zhu F, Muresan L, Benavides-Piccione R, DeFelipe J, Fricker D, Kopanitsa MV, Duncan RR, Klenerman D, Komiyama NH, Lee SF, Grant SGN. 2016. PSD95 nanoclusters are postsynaptic building blocks in hippocampus circuits. *Scientific Reports* **6**:1–14.

Bykov YS, Schaffer M, Dodonova SO, Albert S, Plitzko JM, Baumeister W, Engel BD, Briggs JA. 2017. The structure of the COPI coat determined within the cell. *Elife* **6**:e32493. doi:10.7554/elife.32493

Castaño-Díez D, Kudryashev M, Stahlberg H. 2017. Dynamo Catalogue: Geometrical tools and data management for particle picking in subtomogram averaging of cryo-electron tomograms. *Journal of Structural Biology* **197**:135–144.

Cathala L, Holderith NB, Nusser Z, DiGregorio DA, Cull-Candy SG. 2005. Changes in synaptic structure underlie the developmental speeding of AMPA receptor-mediated EPSCs. *Nature Neuroscience* **8**:1310–1318.

Chen L, Chetkovich DM, Petralia RS, Sweeney NT, Kawasaki Y, Wenthold RJ, Bredt DS, Nicoll RA. 2000. Stargazin regulates synaptic targeting of AMPA receptors by two distinct mechanisms. *Nature* **408**:936–943.

Chen X, Winters C, Azzam R, Li X, Galbraith JA, Leapman RD, Reese TS. 2008. Organization of the core structure of the postsynaptic density. *Proceedings Of The National Academy Of Sciences Of The United States Of America* **105**:4453–4458.

Chua JJE, Kindler S, Boyken J, Jahn R. 2010. The architecture of an excitatory synapse. *Journal of Cell Science* **123**:819–823.

Cooney JR, Hurlburt JL, Selig DK, Harris KM, Fiala JC. 2002. Endosomal compartments serve multiple hippocampal dendritic spines from a widespread rather than a local store of recycling membrane. *Journal of Neuroscience* **22**:2215–2224.

Dani A, Huang B, Bergan J, Dulac C, Zhuang X. 2010. Superresolution imaging of chemical synapses in the brain. *Neuron* **68**:843–856.

Ebrahimi S, Okabe S. 2014. Structural dynamics of dendritic spines: Molecular composition, geometry and functional regulation. *BBA - Biomembranes* **1838**:2391–2398.

El-Husseini AE, Schnell E, Chetkovich DM, Nicoll RA, Bredt DS. 2000. PSD-95 involvement in maturation of excitatory synapses. *Science (New York, NY)* **290**:1364–1368.

Engel BD, Schaffer M, Albert S, Asano S, Plitzko JM, Baumeister W. 2015. In situ structural analysis of Golgi intracisternal protein arrays. *Proceedings Of The National Academy Of Sciences Of The United States Of America* **112**:11264–11269.

Förster F, Medalia O, Zauberman N, Baumeister W, Fass D. 2005. Retrovirus envelope protein complex structure in situ studied by cryo-electron tomography. *Proceedings Of The National Academy Of Sciences Of The United States Of America* **102**:4729–4734.

Frank RAW, Komiyama NH, Ryan TJ, Zhu F, Dell TJO rsquo, Grant SGN. 2016. NMDA receptors are selectively partitioned into complexes and supercomplexes during synapse maturation. *Nature Communications* **7**:11264.

Fukuda Y, Laugks U, Lucic V, Baumeister W, Danev R. 2015. Electron cryotomography of vitrified cells with a Volta phase plate. *Journal of Structural Biology* **190**:143–154.

Gray EG. 1959. Axo-somatic and axo-dendritic synapses of the cerebral cortex: An electron microscope study. *Journal of anatomy* **93**:420–433.

Hagen WJH, Wan W, Briggs JAG. 2017. Implementation of a cryo-electron tomography tilt-scheme optimized for high resolution subtomogram averaging. *Journal of Structural Biology* **197**:191–198.

Hansen KB, Wollmuth LP, Bowie D, Furukawa H, Menniti FS, Sobolevsky AI, Swanson GT, Swanger SA, Greger IH, Nakagawa T, McBain CJ, Jayaraman V, Low C-M, Dell'Acqua ML, Diamond JS, Camp CR, Perszyk RE, Yuan H, Traynelis SF. 2021. Structure, Function, and Pharmacology of Glutamate Receptor Ion Channels. *Pharmacol Rev* **73**:298–487. doi:10.1124/pharmrev.120.000131

Hanson J. 1967. Axial Period of Actin Filaments. *Nature* **213**:353–356. doi:10.1038/213353a0

Harris AZ, Pettit DL. 2007. Extrasynaptic and synaptic NMDA receptors form stable and uniform pools in rat hippocampal slices. *J Physiology* **584**:509–519. doi:10.1113/jphysiol.2007.137679

Harris KM, Weinberg RJ. 2012. Ultrastructure of Synapses in the Mammalian Brain. *Cold Spring Harbor Perspectives in Biology* **4**:a005587–a005587.

Imig C, López-Murcia FJ, Maus L, García-Plaza IH, Mortensen LS, Schwark M, Schwarze V, Angibaud J, Nägerl UV, Taschenberger H, Brose N, Cooper BH. 2020. Ultrastructural Imaging of Activity-Dependent Synaptic Membrane-Trafficking Events in Cultured Brain Slices. *Neuron* **108**:843-860.e8. doi:10.1016/j.neuron.2020.09.004

Kanaseki T, Kadota K. 1969. THE "VESICLE IN A BASKET." *J Cell Biology* **42**:202–220. doi:10.1083/jcb.42.1.202

Kerr JM, Blanpied TA. 2012. Subsynaptic AMPA Receptor Distribution Is Acutely Regulated by Actin-Driven Reorganization of the Postsynaptic Density. *The Journal of Neuroscience* **32**:658–673.

Kononenko NL, Haucke V. 2015. Molecular Mechanisms of Presynaptic Membrane Retrieval and Synaptic Vesicle Reformation. *Neuron* **85**:484–496.

Kremer JR, Mastronarde DN, McIntosh JR. 1996. Computer Visualization of Three-Dimensional Image Data Using IMOD. *Journal of Structural Biology* **116**:71–76.

Kukulski W, Schorb M, Welsch S, Picco A, Kaksonen M, Briggs JAG. 2011. Correlated fluorescence and 3D electron microscopy with high sensitivity and spatial precision. *J Cell Biol* **192**:111–119. doi:10.1083/jcb.201009037

Lowenthal MS, Markey SP, Dosemeci A. 2015. Quantitative Mass Spectrometry Measurements Reveal Stoichiometry of Principal Postsynaptic Density Proteins. *J Proteome Res* **14**:2528–2538. doi:10.1021/acs.jproteome.5b00109

MacGillavry HD, Song Y, Raghavachari S, Blanpied TA. 2013. Nanoscale Scaffolding Domains within the Postsynaptic Density Concentrate Synaptic AMPA Receptors. *Neuron* **78**:615–622.

Martinez-Sanchez A, Laugks U, Kochovski Z, Papantoniou C, Zinzula L, Baumeister W, Lučić V. 2021. Trans-synaptic assemblies link synaptic vesicles and neuroreceptors. *Sci Adv* **7**:eabe6204. doi:10.1126/sciadv.abe6204

Mastronarde DN. 2005. Automated electron microscope tomography using robust prediction of specimen movements. *Journal of Structural Biology* **152**:36–51.

Masugi-Tokita M, Shigemoto R. 2007. High-resolution quantitative visualization of glutamate and GABA receptors at central synapses. *Current Opinion In Neurobiology* **17**:387–393.

Melander JB, Nayebi A, Jongbloets BC, Fortin DA, Qin M, Ganguli S, Mao T, Zhong H. 2021. Distinct in vivo dynamics of excitatory synapses onto cortical pyramidal neurons and parvalbumin-positive interneurons. *Cell Reports* **37**:109972. doi:10.1016/j.celrep.2021.109972

Migaud M, Charlesworth P, Dempster M, Webster LC, Watabe AM, Makhinson M, He Y, Ramsay MF, Morris RG, Morrison JH, O'dell TJ, Grant SG. 1998. Enhanced long-term potentiation and impaired learning in mice with mutant postsynaptic density-95 protein. *Nature* **396**:433–439.

Missler M, Sudhof TC, Biederer T. 2012. Synaptic Cell Adhesion. *Cold Spring Harbor Perspectives in Biology* **4**:a005694–a005694.

Mitchison TJ. 1995. Evolution of a dynamic cytoskeleton. *Philos Trans R Soc Lond Ser B: Biol Sci* **349**:299–304. doi:10.1098/rstb.1995.0117

Nair D, Hosy E, Petersen JD, Constals A, Giannone G, Choquet D, Sibarita J-B. 2013. Super-resolution imaging reveals that AMPA receptors inside synapses are

dynamically organized in nanodomains regulated by PSD95. *Journal of Neuroscience* **33**:13204–13224.

Nakahata Y, Yasuda R. 2018. Plasticity of Spine Structure: Local Signaling, Translation and Cytoskeletal Reorganization. *Frontiers in Synaptic Neuroscience* **10**:1194–13.

Nickell S, Förster F, Linaroudis A, Net WD, Beck F, Hegerl R, Baumeister W, Plitzko JM. 2005. TOM software toolbox: acquisition and analysis for electron tomography. *Journal of Structural Biology* **149**:227–234.

Okamoto K-I, Narayanan R, Lee SH, Murata K, Hayashi Y. 2007. The role of CaMKII as an F-actin-bundling protein crucial for maintenance of dendritic spine structure. *Proc National Acad Sci* **104**:6418–6423. doi:10.1073/pnas.0701656104

Park M. 2018. AMPA Receptor Trafficking for Postsynaptic Potentiation. *Frontiers in Cellular Neuroscience* **12**:59–10.

Penn AC, Zhang CL, Georges F, Royer L, Breillat C, Hosy E, Petersen JD, Humeau Y, Choquet D. 2017. Hippocampal LTP and contextual learning require surface diffusion of AMPA receptors. *Nature* **549**:384–388.

Peters A, Palay SL, Webster HF. 1970. The fine structure of the nervous system: the cells and their processes.

Pettersen EF, Goddard TD, Huang CC, Couch GS, Greenblatt DM, Meng EC, Ferrin TE. 2004. UCSF Chimera—A visualization system for exploratory research and analysis. *J Comput Chem* **25**:1605–1612. doi:10.1002/jcc.20084

Pollard TD, Mooseker MS. 1981. Direct measurement of actin polymerization rate constants by electron microscopy of actin filaments nucleated by isolated microvillus cores. *The Journal of Cell Biology* **88**:654–659.

Regan MC, Romero-Hernandez A, Furukawa H. 2015. A structural biology perspective on NMDA receptor pharmacology and function. *Curr Opin Struc Biol* **33**:68–75. doi:10.1016/j.sbi.2015.07.012

Roy M, Sorokina O, Skene N, Simonnet C, Mazzo F, Zwart R, Sher E, Smith C, Armstrong JD, Grant SGN. 2017. Proteomic analysis of postsynaptic proteins in regions of the human neocortex. *Nat Neurosci* **21**:1–9. doi:10.1038/s41593-017-0025-9

Rusakov DA, Savtchenko LP, Zheng K, Henley JM. 2011. Shaping the synaptic signal: molecular mobility inside and outside the cleft. *Trends In Neurosciences* **34**:359–369.

Schorb M, Briggs JAG. 2014. Correlated cryo-fluorescence and cryo-electron microscopy with high spatial precision and improved sensitivity. *Ultramicroscopy* **143**:24–32. doi:10.1016/j.ultramic.2013.10.015

Sheng M, Kim E. 2011. The Postsynaptic Organization of Synapses. *Csh Perspect Biol* **3**:a005678. doi:10.1101/cshperspect.a005678

Smith MF, Langmore JP. 1992. Quantitation of molecular densities by cryo-electron microscopy Determination of the radial density distribution of tobacco mosaic virus. *J Mol Biol* **226**:763–774. doi:10.1016/0022-2836(92)90631-s

Sobolevsky A, Rosconi M, Gouaux E. 2009. X-ray structure, symmetry and mechanism of an AMPA-subtype glutamate receptor. *Nature*.

Spruston N, Jonas P, Sakmann B. 1995. Dendritic glutamate receptor channels in rat hippocampal CA3 and CA1 pyramidal neurons. *J Physiology* **482**:325–352. doi:10.1113/jphysiol.1995.sp020521

Tajima N, Karakas E, Grant T, Simorowski N, Diaz-Avalos R, Grigorieff N, Furukawa H. 2016. Activation of NMDA receptors and the mechanism of inhibition by ifenprodil. *Nature* **534**:63–68.

Tang A-H, Chen H, Li TP, Metzbower SR, MacGillavry HD, Blanpied TA. 2016. A trans-synaptic nanocolumn aligns neurotransmitter release to receptors. *Nature* **536**:210–214.

Tao C-L, Liu Y-T, Sun R, Zhang B, Qi L, Shivakoti S, Tian C-L, Zhang P, Lau P-M, Zhou ZH, Bi G-Q. 2018. Differentiation and Characterization of Excitatory and Inhibitory Synapses by Cryo-electron Tomography and Correlative Microscopy. *J Neurosci* **38**:1493–1510. doi:10.1523/jneurosci.1548-17.2017

Tønnesen J, Inavalli VVGK, Nägerl UV. 2018. Super-Resolution Imaging of the Extracellular Space in Living Brain Tissue. *Cell* **172**:1108-1121.e15. doi:10.1016/j.cell.2018.02.007

Turk M, Baumeister W. 2020. The promise and the challenges of cryo electron tomography. *Febs Lett* **594**:3243–3261. doi:10.1002/1873-3468.13948

Volgushev M, Vidyasagar TR, Chistiakova M, Eysel UT. 2000. Synaptic transmission in the neocortex during reversible cooling. *NSC* **98**:9–22.

Wagner T, Merino F, Stabrin M, Moriya T, Antoni C, Apelbaum A, Hagel P, Sitsel O, Raisch T, Prumbaum D, Quentin D, Roderer D, Tacke S, Siebolds B, Schubert E, Shaikh TR, Lill P, Gatsogiannis C, Raunser S. 2019. SPHIRE-crYOLO is a fast and accurate fully automated particle picker for cryo-EM. *Communications Biology* 1–13.

Wan W, Kolesnikova L, Clarke M, Koehler A, Noda T, Becker S, Briggs JAG. 2017. Structure and assembly of the Ebola virus nucleocapsid. *Nature* **51**:394–397.

Watanabe S, Trimbuch T, Camacho-Pérez M, Rost BR, Brokowski B, Söhl-Kielczynski B, Felies A, Davis MW, Rosenmund C, Jorgensen EM. 2014. Clathrin regenerates synaptic vesicles from endosomes. *Nature* **515**:228–233.

Whittaker VP. 1959. The isolation and characterization of acetylcholine-containing particles from brain. *Biochem J* **72**:694–706. doi:10.1042/bj0720694

Wolf SG, Mutsafi Y, Dadosh T, Ilani T, Lansky Z, Horowitz B, Rubin S, Elbaum M, Fass D. 2017. 3D visualization of mitochondrial solid-phase calcium stores in whole cells. *eLife* **6**:147.

Zhu F, Cizeron M, Qiu Z, Benavides-Piccione R, Kopanitsa MV, Skene NG, Koniaris B, DeFelipe J, Fransén E, Komiyama NH, Grant SGN. 2018. Architecture of the Mouse Brain Synaptome. *Neuron* **99**:781–799.

Zhu S, Gouaux E. 2017. Structure and symmetry inform gating principles of ionotropic glutamate receptors. *Neuropharmacology* **112**:11–15. doi:10.1016/j.neuropharm.2016.08.034

Zuber B, Nikonenko I, Klauser P, Muller D, Dubochet J. 2005. The mammalian central nervous synaptic cleft contains a high density of periodically organized complexes. *Proceedings Of The National Academy Of Sciences Of The United States Of America* **102**:19192–19197.

Acknowledgements

We would like to thank Christos Savvas, Giuseppe Cannone and Shaoxia Chen for help with maintaining and setting up MRC LMB Titan Krios microscopes. We would like to thank the Astbury Biostructure Laboratory (ABSL), particularly Rebecca Thompson, Emma Hesketh, Dan Maskell, and Helmut Gnaegi for help with setting up and maintaining HPF, cryo-ultramicrotome, cryoFM and Titan Krios microscopes. We are grateful to Jake Grimmett and Toby Darling for providing essential computational support. Heather Lloyd and Biomedical staff for technical support. Madeleine Gilbert and Eva Martínez Barceló for assistance with annotation of synapse tomograms. Grant funding: An Academy of Medical Sciences Springboard Award, a University of Leeds Academic Fellowship, and UKRI Future Leader Fellowship (MR/V022644/1) to RAWF. A BBSRC White Rose DTP studentship (BB/M011151/1) to CLo. A Wellcome Trust (Technology Development Grant 202932), the European Research Council (ERC) under

the European Union’s Horizon 2020 Research and Innovation Programme (695568 SYNNOVATE), Simons Foundation for Autism Research Initiative (529085) to SGGN and NHK. Medical Research Council (MC_UP_1201/16), the European Research Council (ERC) under the European Union's Horizon 2020 research and innovation programme (ERC-CoG-648432 MEMBRANEFUSION), and the Max Planck Society to JAGB. WK was supported by the Medical Research Council (MC_UP_1201/8). ABSL Titan Krios microscopes were funded by the University of Leeds and Wellcome Trust (108466/Z/15/Z). The Leica EM ICE, UC7 ultra/cryo-ultramicrotome and cryoCLEM systems were funded by Wellcome Trust (208395/Z/17/Z).

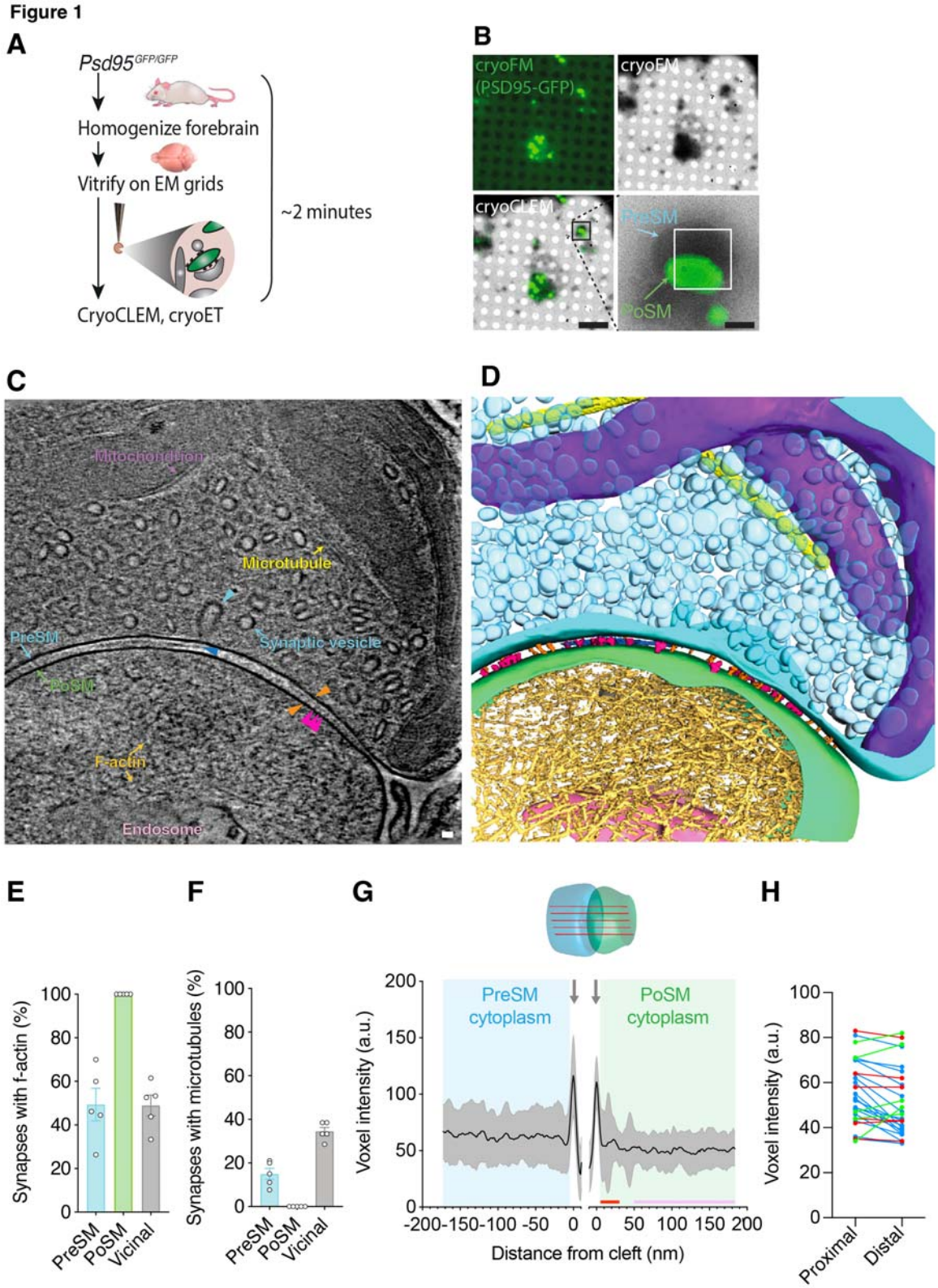

Figure 1. CryoCLEM-targeted cryoET of mouse forebrain synapses.

(A) Schematic of the 'ultra-fresh' preparation of synapses for cryoCLEM. *Psd95*$^{GFP/GFP}$ knockin mice were culled, forebrain was dissected, homogenized in ice cold artificial cerebrospinal fluid, and plunge-frozen on cryoEM grids. 2 minutes was the time taken to cull, dissect and cryopreserve samples on EM grids.

(B) CryoCLEM of cryoEM grid square containing an ultra-fresh synapse preparation. *Top left*, cryoFM image of a holey carbon grid square. *Top right*, cryoEM image of the same grid square shown in top left. *Bottom left*, merged image of cryoFM and cryoEM images indicating location of PSD95-GFP puncta. Scale bar, 5 µm. Black box indicates region enlarged in *Bottom right*, showing PSD95-GFP associated with PoSM. White rectangle, indicates region where images for the tomogram shown in C were acquired. Scale bar, 500 nm.

(C) Tomographic slice of PSD95-contaning glutamatergic synapse. The PoSM (green) was identified by PSD-GFP cryoCLEM and the PreSM (cyan) was identified by its tethering to the PoSM and the prevalence of synaptic vesicles. Salient organelle and macromolecular constituents are indicated: Purple arrow, mitochondrion. Yellow arrow, microtubule. Cyan arrow, synaptic vesicle and cyan arrowhead indicating intermediate of vesicle fission/fusion. Gold arrow, F-actin filament. Pink arrow, putative endosomal compartment. Orange arrowheads, transsynaptic macromolecular complex bridging PreSM and PoSM. Magenta arrowheads, postsynaptic membrane proteins with extracellular domains extending 13-14 nm into the synaptic cleft. Blue arrow, lateral matrix of macromolecules in synaptic cleft. Scale bar, 20 nm. The tomographic map shown here is representative of 93 tomograms obtained across 5 mouse forebrain preparations.

(D) 3D segmentation of membranes and macromolecules in a representative tomographic volume of a PSD95-containing glutamatergic synapse. Coloured as in C.

(E) Prevalence of branched filamentous actin networks in presynaptic membrane compartments (PreSM, cyan), PSD95-containing postsynaptic membrane compartments (PoSM, green), and neighbouring non-synaptic membrane compartments (Vicinal, grey).

Data points are per mouse, for 5 adult *Psd95*$^{GFP/GFP}$ mouse forebrain samples. Error bars, SEM.

(F) Same as E but for microtubules.

(G) Molecular crowding of the PreSM and PoSM cytoplasm in ultra-fresh synapse preparation. *Top*, schematic showing the measurement of molecular density estimated with multiple line profiles plots of voxel intensity within each synapse tomogram. *Bottom*, voxel intensity (a.u., arbitrary units) profile plots of presynaptic (cyan) and postsynaptic (green) cytoplasm. Profiles were aligned to the lipid membrane peak of the PreSM and PoSM (grey arrows). The average intensity profile of 27 synapses from 3 mice is shown in black with 1 standard deviation in grey. Red and purple bar, proximal and distal regions of PoSM cytoplasm, respectively, as analysed in H.

(H) Comparison of average molecular density profile in regions 5-30 nm (proximal) and 50-200 nm (distal) from the PoSM of each synapse. Regions proximal to the PoSM correspond to locations in which a PSD is a conserved feature in conventional EM. Blue, red and green datapoints, synapses with cytoplasm proximal the PoSM that contained significantly higher, lower, and not significantly different density from distal regions, respectively (two-tailed *t* test with Bonferroni correction, $P < 0.05$, n=682 and 5673 voxels).

Figure supplement 1. CryoFM, docked vesicles and actin in PSD95-GFP-containing synapses.

Figure supplement 2. Molecular density analysis within synapse tomographic volumes.

Figure supplement 3. Tomographic slices and molecular density profiles of 27 ultra-fresh PSD95-GFP synapses.

Figure 1–video 1-7. Reconstructed tomographic volumes of PSD95-GFP-containing ultra-fresh synapses.

Figure 1-table 1. A spreadsheet detailing the organelle and macromolecular constituents within each tomogram of the ultra-fresh synapse cryoET dataset, including within the PreSM and PoSM of PSD95-GFP containing synapses and additional subcellular compartments in the vicinity.

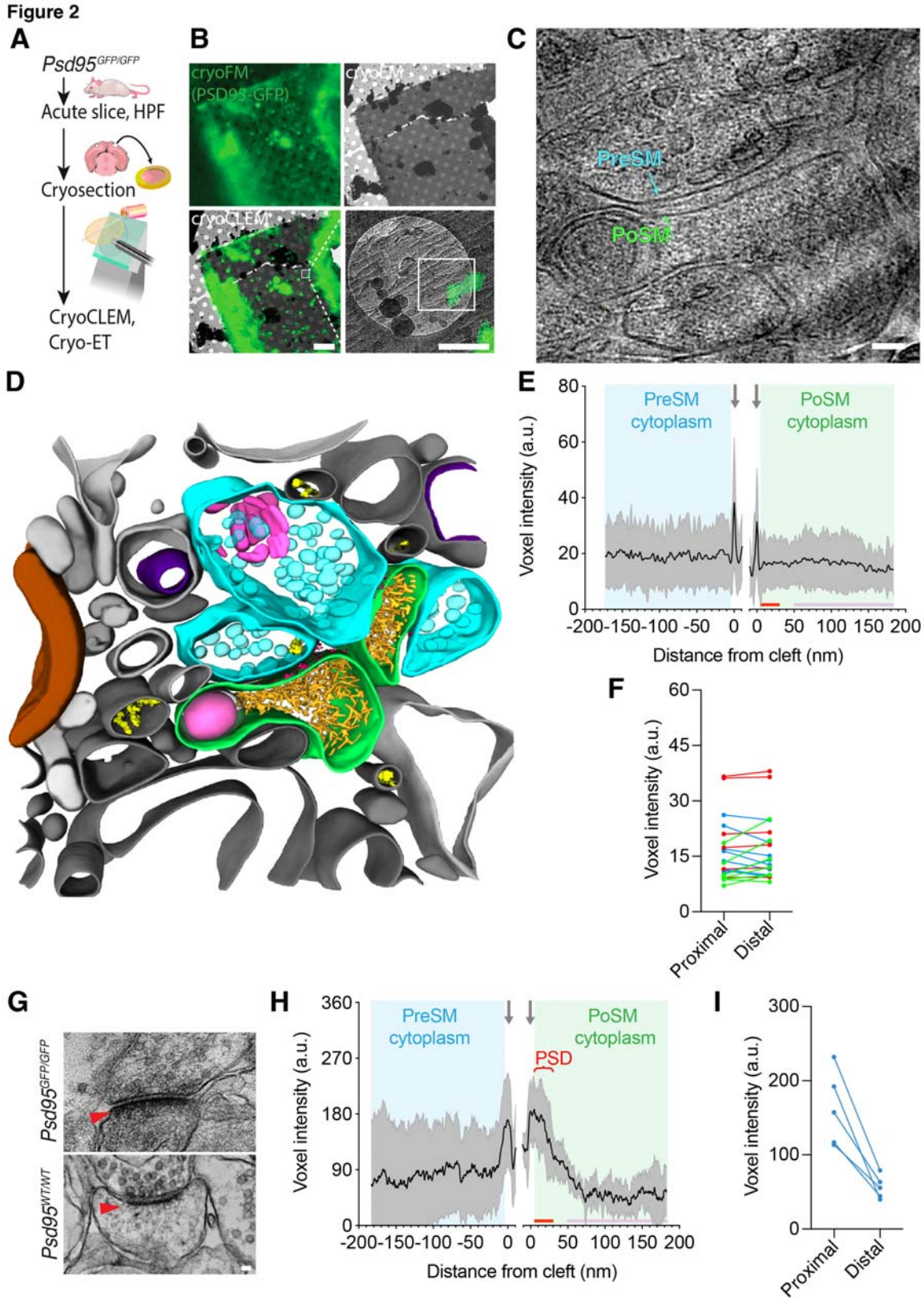

Figure 2. The in-tissue molecular architecture of glutamatergic synapses in the adult mammalian brain.

(A) Schematic showing cryoCLEM and cryoET workflow using thin vitreous sections from forebrains of adult *Psd95*$^{GFP/GFP}$ knockin mice to determine the in-tissue architecture of glutamatergic synapses. Mice were culled and dissected. 100 µm acute slices were collected, from which 2 mm diameter biopsies of cortex were high-pressure frozen. 70-150 nm thin cryo-sections were cut from vitrified tissue and attached to cryoEM grid for cryoCLEM and cryoET.

(B) CryoCLEM of cryoEM grid square containing 150 nm thin cryo-section. *Top left*, cryoFM image of a holey carbon grid square. *Top right*, cryoEM image of the same grid square shown in top left. *Bottom left*, merged image of cryoFM and cryoEM images indicating location of PSD95-GFP puncta. Scale bar, 5 µm. Black box indicates region enlarged in *Bottom right*, showing PSD95-GFP associated with PoSM. White box indicates region where images for the tomogram shown in 'c' were acquired. Scale bar, 500 nm.

(C) Tomographic slice of PSD95-GFP containing synapse within thin vitreous cryo-section of adult mouse cortex. Cyan, PreSM. Green, PoSM. Scale bar, 50 nm.

(D) 3D segmentation of membranes and macromolecules in a representative tomographic volume of a PSD95-containing glutamatergic synapse within thin vitreous cryo-section of adult mouse cortex. The PoSM (green) was identified by PSD-GFP cryoCLEM and the PreSM (cyan) was identified by its tethering to the PoSM and the prevalence of synaptic vesicles. Salient organelle and macromolecular constituents are indicated: Magenta, membrane proteins within synaptic cleft. Purple, mitochondrion. Yellow, microtubule. Pink, putative endosomal compartment. Brown, myelin. Grey, vicinal membrane-bound subcellular compartments.

(E) Molecular profiles same as **Figure 1G** but for 21 in-tissue synapses of vitreous cryo-sections from acute brain slices of seven *Psd95*$^{GFP/GFP}$ mice.

(F) Comparison of average molecular density profile in regions 5-30 nm (proximal) and 50-200 nm (distal) from the PoSM of each synapse. Blue, red and green datapoints, synapses with cytoplasm proximal the PoSM that contained significantly higher, lower,

and not significantly different density from distal regions, respectively (two-tailed *t* test with Bonferroni correction, $P < 0.05$, n=682 and 5673 voxels).

(G) Conventional EM of synapses in chemically fixed, resin-embedded, heavy metal-stained acute brain slice biopsies from *Psd95*$^{GFP/GFP}$ knockin (left) and wildtype (right), respectively. Red arrowhead, postsynaptic density. Scale bar, 50 nm.

(H and I) Same as e and f but for acute brain slice biopsies imaged by conventional EM (chemically fixed, resin imbedded, and heavy metal-stained) from 3 *Psd95*$^{GFP/GFP}$ mice. PSD, postsynaptic density evident in non-native, conventional EM samples.

Figure supplement 1. Molecular density profiling and tomographic slices of 21 in-tissue cryosection tomograms containing PSD95-GFP synapses.

Figure supplement 2. Conventional EM of adult brain glutamatergic synapses.

Figure 2–video 1-2. Reconstructed tomographic volumes of in-tissue PSD95-GFP-containing synapses.

Figure 2-table 1. A spreadsheet detailing the organelle and macromolecular constituents within each tomogram of the in-tissue synapse cryoET dataset, including within the PreSM and PoSM of PSD95-GFP containing synapses and additional subcellular compartments in the vicinity.

Figure 3

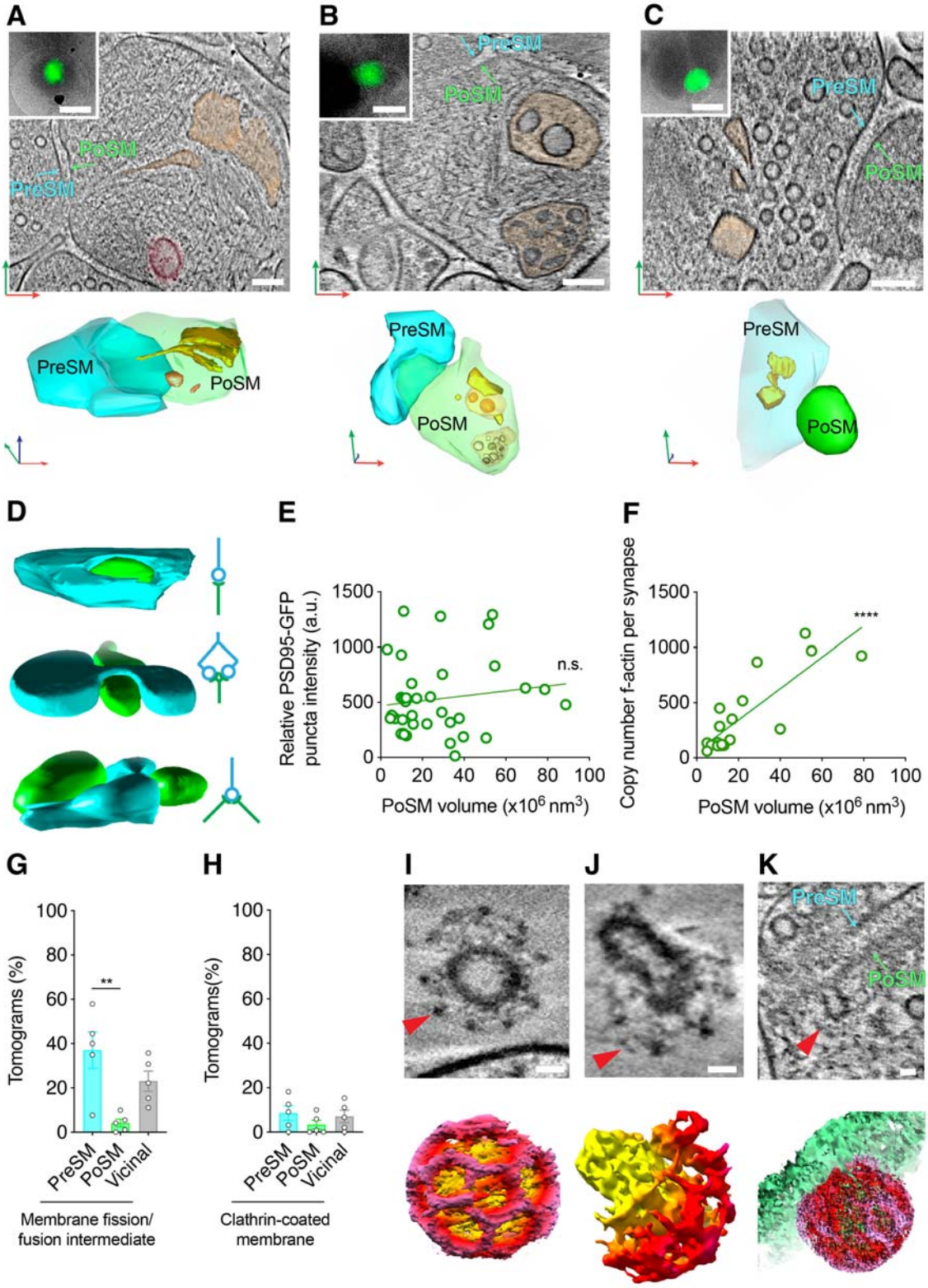

Figure 3. Architecture of lipid membrane bilayers in glutamatergic synapses.

(A-C) Organelles in PSD95-containing synapse shown *top*, as a tomographic slice and *bottom*, 3D segmentation. *Top inset*, PSD95-GFP cryoCLEM image of synapse. Scale bar, 500 nm. Cyan, PreSM. Green, PoSM. Red, green and blue arrows indicate *x*-, *y*-, and *z*-axis of tomogram, respectively. Scale bar, 100 nm.

(A) Flat/tubular membrane compartment and large spheroidal membrane compartment pseudo-coloured orange and red, respectively.

(B) Multivesicular bodies pseudo-coloured orange.

(C) Polyhedral membrane vesicle pseudo-coloured orange

(D) 3D segmentation (*left*) and schematic (*right*) of PSD95-GFP-containing synapses showing various topologies of connectivity. *Top*, unimodal single input and single output. *Middle*, bifurcated synapse with single input and output. *Bottom*, divergent synapse with single input and two outputs. Cyan, PreSM input. Green, PoSM output.

(E) Plot of fluorescence intensity (from cryoFM of PSD95-GFP) versus PoSM volume suggesting that there is no correlation between apparent amount of PSD95-GFP and PoSM volume. Linear regression (green line) with Pearson's r=0.14, P=0.41.

(F) Plot showing the copy number of F-actin cytoskeletal elements in PoSM compartment versus PoSM volume of each synapse. The copy number of actin filaments was estimated from 3D segmented models of 7 nm filaments within the tomographic map. F-actin branching from another filament were counted as a separate filament. Linear regression (green line) with Pearson's r=0.83, P<0.0001.

(G-K) Snapshots of membrane remodeling within glutamatergic synapses.

(G) Prevalence of membrane fission/fusion intermediates within PreSM, PoSM, and non-synaptic membranes (vicinal) from tomograms of 5 adult $Psd95^{GFP/GFP}$ mice. Error bars, SEM.

(H) Same as E but for clathrin-coated membrane.

(I) *Top*, tomographic slice of a clathrin-coated (red arrowhead) synaptic vesicle and *bottom*, a 3D tomographic density map for the region shown on top. Clathrin cage and membrane is shown with red and yellow voxels respectively. Scale bar, 20 nm.

(J) *Top*, tomographic slice of a clathrin-coat (red arrowhead) encapsulating part of an internal membrane within the PreSM compartment of a PSD95-GFP containing synapse and shown *bottom*, a masked 3D tomographic map. Clathrin cage and membrane is shown with red and yellow voxels, respectively. Scale bar, 20 nm.

(K) *Top*, tomographic slice, and *bottom*, masked 3D tomographic map showing clathrin-coated endocytic pit (red arrowhead) within the cleft of a PSD95-GFP containing PoSM. Clathrin cage and membrane is shown with red and green voxels, respectively. Scale bar, 20 nm.

Figure supplement 1. Structural categories of membrane-bound organelles in PSD95-containing synapses in the adult brain.

Figure 4

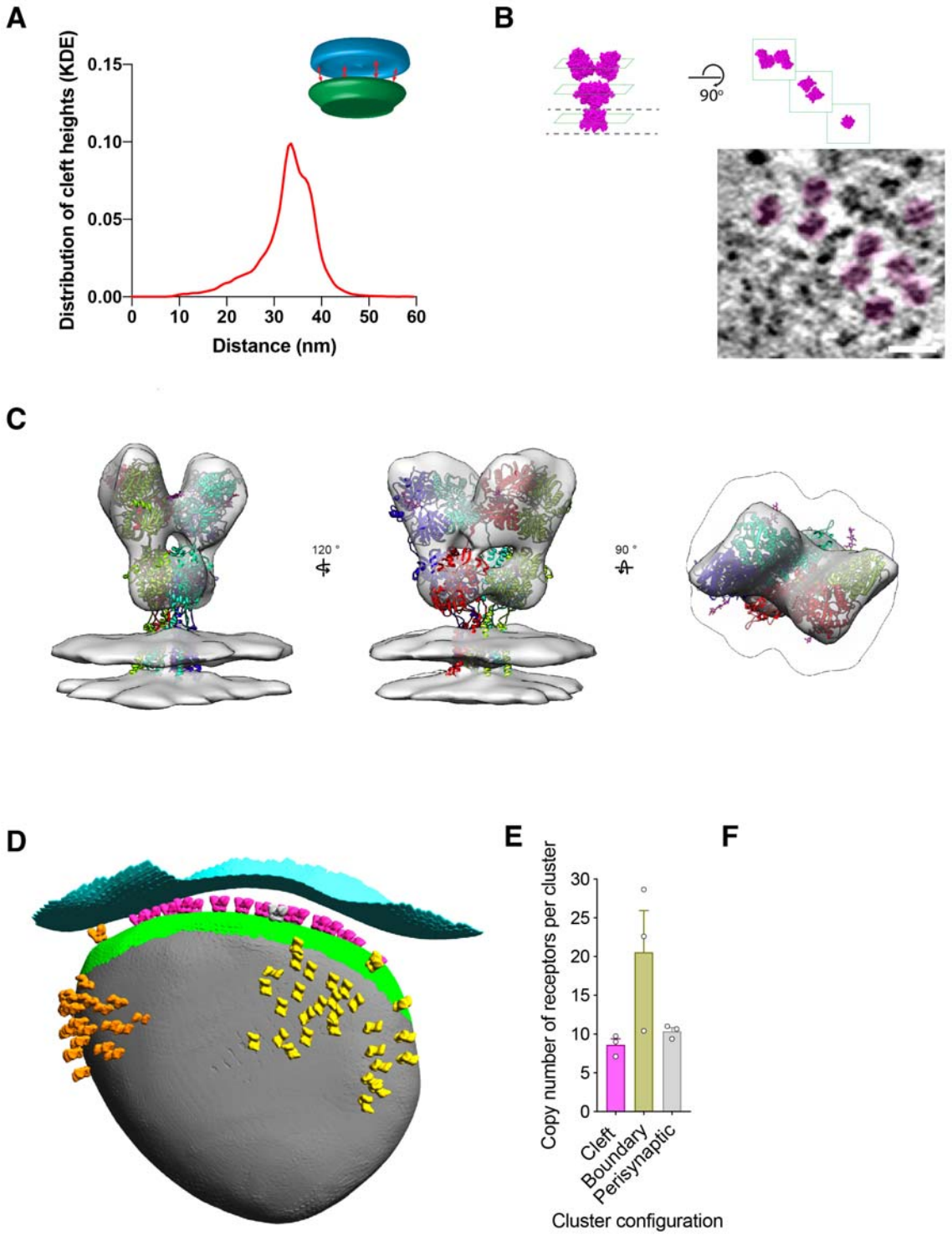

Figure 4. Structural variables of synaptic strength.

(A) Distribution of cleft height distances of all synapses is shown as a kernel density estimation (KDE). *Inset*, schematic depicting nearest neighbour method for defining the synaptic cleft between PreSM (cyan) and PoSM (green) compartments.

(B) *Top left*, 'side' view of atomic structure of AMPA subtype of ionotropic glutamate receptor (PDB ID: 3kg2). Dashed line, boundary of transmembrane domain. *Top right*, 'top' views of distal amino-terminal domain layer, proximal ligand-binding domain layer, and transmembrane domain layer. *Bottom left*, tomographic slice of PSD95-GFP containing membrane oriented approximately parallel to the electron beam. Putative ionotropic glutamate receptor pseudo-coloured in magenta. *Bottom right*, tomographic of PSD95-GFP containing membrane oriented approximately orthogonal to the electron beam. Multiple putative ionotropic glutamate receptor pseudo-coloured in magenta. Scale bar, 20 nm.

(C) In situ structure of ionotropic glutamate receptors within PSD95-GFP containing PoSM determined by subtomogram averaging of 2,368 sub-volumes. Atomic model of AMPA receptor (GluA2, PDB: 3kg2) docked in the determined map. Subunits of the model are coloured in red, yellow, cyan and purple.

(D) Cluster analysis of identified ionotropic glutamate receptors depicted as a 3D model of the postsynaptic compartment with ionotropic glutamate receptors in the orientation and position determined by sub-tomogram averaging. Each cluster is coloured differently: magenta, orange, and yellow. Presynaptic and postsynaptic cleft membrane are shown in cyan and green, respectively. Postsynaptic membrane outside of the cleft is shown in grey.

(E) Receptor number per cluster for three different cluster locations: in the cleft (magenta), partly inside and outside the cleft (boundary, yellow), and completely outside the cleft (perisynaptic, grey) from tomograms of 3 adult $Psd95^{GFP/GFP}$ mice.

(F) Prevalence of receptor clusters for three different cluster locations: in the cleft (magenta), partly inside and outside the cleft (boundary, yellow), and completely outside the cleft (perisynaptic, grey) from tomograms of 3 adult $Psd95^{GFP/GFP}$ mice.

Figure supplement 1. Quantification and variability of cleft height in glutamatergic synapses.

Figure supplement 2. Subtomogram averaging and anchoring of ionotropic glutamate receptors.

Methods

Mouse genetics and breeding

Animals were treated in accordance with UK Animal Scientific Procedures Act (1986) and NIH guidelines. The generation and characterization of the PSD95-GFP knockin mouse (*Psd95*^{GFP}) was described (Broadhead et al., 2016; Zhu et al., 2018). The endogenous PSD95 protein levels, assembly into supercomplexes, anatomical localization, developmental timing of expression and electrophysiological function in the hippocampus CA1-CA3 synapses in *Psd95*^{GFP} mice are indistinguishable from WT mice (Broadhead et al., 2016; Frank et al., 2016; Zhu et al., 2018).

Ultra-fresh synapse preparation

Samples were prepared from 5 adult (P65-P100) male *Psd95*$^{GFP/GFP}$ knockin mice. Sample preparation from culling to cryopreservation of each mouse was less than 2 minutes. Mice were culled by cervical dislocation. Forebrain, including cortex and hippocampus, that encompass the known diversity glutamatergic synapses (Zhu et al., 2018) were removed (in <40 s) and were homogenized (<20 s) by applying 12 strokes of a Teflon-glass pestle and mortar containing 5 ml ice-cold (~1 °C) carbogenated (5% CO_2, 95% O_2) artificial cerebrospinal fluid (ACSF; 125 mM NaCl, 25 mM KCl, 25 mM $NHCO_3$, 25 mM glucose, 2.5 mM KCl, 2 mM $CaCl_2$, 1.25 mM NaH_2PO_4, 1 mM $MgCl_2$; Osmolality: 310 mOsM/L). Ice-cold ACSF was used to limit mechanical stimulation since synaptic transmission and other enzyme-catalyzed processes (e.g. endocytosis) are negligible at this temperature(Volgushev et al., 2000). 1 µl homogenate was diluted into 100 µl ice-cold ACSF containing 1:6 BSA-coated 10 nm colloidal gold (BBA; used as a fiducial maker) (<10 s). 3 µl sample was applied onto glow-discharged 1.2/1.3 carbon foil supported by 300-mesh Au or Cu grids (Quantifoil) held at 4°C, 100% humidity in Vitrobots (Mark IV, Thermo Fisher). Excess sample was manually blotted from the non-foil side of the grid for ~4s with Whatman paper (No. 1; manipulated within the Vitrobot with tweezers) before cryopreserving by plunge freezing in liquid ethane held at -180°C (*57*). 1-2 grids were prepared from each mouse on 1-2 Vitrobots.

In-tissue acute slice synapse preparation

Samples were prepared from 7 adult (P65-P100) male *Psd95*$^{EGFP/EGFP}$ knockin mice. Mice were culled by cervical dislocation. Forebrain, including cortex and hippocampus, were removed and 100 µm coronal acute slices were prepared in cutting buffer (93 mM N-methyl-D-glucamine, 2.5 mM KCl, 1.2 mM NaH2PO4, 30 mM NaHCO3, 20 mM HEPES, 5 mM Sodium ascorbate, 2 mM Thiourea, 3 mM Sodium Pyruvate, 10 mM MgSO4, 0.5 mM CaCl2, pH 7.39-7.40, osmolarity 305-315 mOsm/L) using a Leica VT1200S vibratome at 0.5-2°C. Tissue biopsies of acute slices were collected following the method established by Zuber and co-workers in which samples remain viable(Zuber et al., 2005). Briefly, slices were recovered in ACSF perfused with carbogen at room temperature for 45 minutes. Next, biopsies were collected with a 2 mm biopsy punch and were transferred to carbogenated NMDG cutting buffer supplemented with 20% dextran 40,000. Biopsies were high-pressure frozen within cryoprotectant into 3 mm carriers using a Leica EM ICE. Vitreous tissue was cut into 70-150 nm thick sections using a Leica FC7 cryo-ultramicrotome with a CEMOVIS diamond knife (Diatome) from regions of the tissue that were ~25 µm from the vibratome cutting edge. Tissue cryo-sections were attached to cryoEM grids at -150°C.

Cryogenic correlated light and electron microscopy

Cryogenic fluorescence microscopy (cryoFM) was performed on the Leica EM cryoCLEM system with a HCX PL APO 50x cryo-objective with NA = 0.9 (Leica Microsystems), an Orca Flash 4.0 V2 sCMOS camera (Hamamatsu Photonics), a Sola Light Engine (Lumencor) and the following filters (Leica Microsystems): green (L5; excitation 480/40, dichroic 505, emission 527/30), red (N21; excitation 515-560, dichroic 580, emission LP 590), and far-red (Y5; excitation 620/60, dichroic 660, emission 700/75). During imaging, the humidity of the room was controlled to 20-25% and the microscope stage was cooled to -195°C. Ice thickness was assessed with a brightfield

image and L5 filter. Regions of the grid with thin ice (~50%) were imaged sequentially with the following channel settings: 0.4 s exposure, 30% intensity in green channel; 40 ms exposure, intensity 11% in BF channel; 0.4 s exposure, 30% intensity in red channel, 0.4 s exposure, 30% intensity in far-red channel. 0.3 µm separated z-stack of images was collected for each channel over a 5-20 µm focal range. Images were processed in Fiji. The location of PSD95-GFP was evident as puncta of varying brightness that were exclusively in the green channel. The occasional autofluorescent spot was identifiable by fluorescence across multiple channels, including green and red channels. Grid squares were selected for cryoCLEM that contained PSD95-GFP puncta within the holes of the holey carbon grid.

Cryogenic electron microscopy and tomography

CryoEM and CryoET data collection was performed on a Titan Krios microscope (FEI) fitted with a Quantum energy filter (slit width 20 eV) and a K2 direct electron detector (Gatan) running in counting mode with a dose rate of ~4 e^-/pixel/second at the detector level during tilt series acquisition. Intermediate magnification EM maps of the selected grid squares were acquired at a pixel size of 5.1 nm. Using these intermediate magnification maps of each grid square and the corresponding cryoFM image, the location of PSD95-GFP puncta was manually estimated; performing computational alignment of cryoFM and cryoEM images before tomogram acquisition was not necessary.

An unbiased tomographic data collection strategy was followed guided by the location PSD95-GFP cryoCLEM data. 93 ultra-fresh and 51 acute slice/in-tissue PSD95-GFP tomograms were collected from 5 and 8 mice respectively. No PSD95-GFP tomograms were excluded from the dataset. Tomographic tilt series of the cryoFM-correlated PSD95-GFP locations were collected between ±60° using a grouped dose-symmetric tilt scheme(Hagen et al., 2017) in serialEM(Mastronarde, 2005) and a phase plate(Fukuda et al., 2015) pre-conditioned for each tomogram. Groups of 3 images with 2° increments were collected. Images with a 2 s exposure with 0.8-1.25 µm nominal defocus, at a dose rate of ~0.5 e^-/Å/s were collected as 8x 0.25 s fractions, giving a total dose ~60 e^-/Å over

the entire tilt series at a calibrated pixel size of 2.89 Å. This pixel size corresponds to a field of view of 1.3 μm^2. Consequently, the centres of all synapses were captured in the tomographic dataset and synapses with a maximum dimension under 1.3 μm were contained entirely within the tomogram. Tomograms of thin vitreous sections were collected with the same protocol but replacing the phase plate with 100 μm objective aperture and acquiring tilt series images at 5-6 μm nominal defocus with a nominal pixel size of 3.42 Å.

Conventional EM

Samples were prepared from adult (P65-P100) male *Psd95*$^{EGFP/EGFP}$ knockin and wildtype mice from three sources: i) Fresh 2 mm diameter biopsy samples of the primary or secondary somatosensory cortex were collected from acute brain slices (as described above) were fixed with chemi-fix buffer composed of 4% paraformaldehyde 2% glutaraldehyde in 50 mM phosphate (PB) pH7.4 for 1 hour. ii) Ultra-fresh synapses were prepared (as described above) and incubated in chemi-fix buffer for 40 min at room temperature. iii) Anesthetized mice were cardiac perfused with 20 ml PB, followed by 40 ml chemi-fix buffer. 100 μm coronal sections were collected from the whole brain with a vibratome, from which 2 mm biopsy samples of the cortex were collected and incubated in chemi-fix buffer at 4°C overnight.

All samples were next washed three times in PB for 1 minute before post-fixation in 2% osmium tetroxide for 1 hour at room temperature. Next, samples were washed three times in PB for 1 minute each and once in 50% ethanol for 1 minute. Samples were next stained with 4% w/v uranyl acetate in 70% for 1 hour at room temperature before dehydration with sequential washes in 70% ethanol, 90% ethanol, 100% ethanol, 100% acetone for 5 minutes each. Samples were resin embedded by washing twice with propylene oxide for 20 minutes before incubation in 50% araldite epoxy resin in propylene oxide at room temperature overnight. Finally, samples were incubated twice in epoxy resin for 10-16 hours before the resin was polymerized in a mold at 60 °C for 3 days. Ultrathin (80-100 nm) sections collected from with an ultramicrotome were placed on 3.05-mm copper

grids, stained with saturated uranyl acetate for 30 minutes, and Reynold's lead citrate for 5 minutes and imaged on a Tecnai F20 TEM at 5,000x and 29,000x magnification.

CryoCLEM image processing

Computational correlation between the cryoFM and cryoEM images was conducted using custom Matlab (Mathworks) scripts as described previously (Kukulski et al., 2011; Schorb and Briggs, 2014). The centre points of at least 10 holes in the holey-carbon foil around each PSD95 position were used as fiducial markers to align the green channel cryoFM image to a montaged intermediate magnification EM image covering the whole grid square. All GFP puncta correlated within membrane-bound compartments with an apparent presynaptic membrane attached to the postsynaptic membrane. The identity of presynaptic membranes was confirmed by the presence of numerous synaptic vesicles.

To quantify relative amount of PSD95 in each synapse, PSD95-EGFP puncta in cryoFM images were segmented using the watershed algorithm in ImageJ, from which the pixel intensities of each puncta were integrated.

Tomogram reconstruction

Frames were aligned and ultra-fresh synapse tomograms were reconstructed using 10-20 tracked 10 nm fiducial gold markers in IMOD (Kremer et al., 1996). Tomograms of synapses in thin vitreous cryo-sections were aligned by patch tracking and denoised using SPIRE-crYOLO (Wagner et al., 2019). Tomograms used for figures, particle picking, annotation of macromolecular constituents and molecular density analysis were generated with 5 iterations of SIRT and binned to a 11.94 Å (binned 4x). Weighted back-projection tomograms (binned 4x and 2x) were used for subtomogram averaging (see below).

Annotation and analysis of macromolecular constituents in tomograms

Annotation described in **Figure 1–table 1** was performed blind by two curators to assess ultra-fresh synapse structures. First, each curator annotated all SIRT reconstructed tomograms independently. Next, a third curator inspected and certified each annotation.

The PoSM was identified using PSD95-GFP cryoCLEM (see above). The PreSM was identified as the membrane compartment attached to the PoSM via transsynaptic adhesion proteins and containing numerous synaptic vesicles. Docked synaptic vesicles were defined as vesicles connected 2-8 nm from the PreSM via macromolecular tethers. The average diameter of vesicles was 40.2 nm and the minimum and maximum dimensions ranged from 20 to 57.8 nm, measured from the outside of the vesicle that included ellipsoidal synaptic vesicles similar to those previously reported (Tao et al., 2018). To assess potential mechanical damage to the native architecture of ultra-fresh synapses, the PoSM or PreSM compartment categorized as either open or closed. An open PreSM or PoSM compartment indicated that the plasma membrane was ruptured, whereas closed PreSM and PoSM compartments were similar to structures obtained from tissue cryo-sections, indicating the native architecture was retained. Only synapses tomograms with closed PreSM or PoSM were used for further analysis of the molecular architecture and constituents of synapses.

Organelles, intermediates of membrane fission or fusion, and identifiable macromolecules were annotated within the presynaptic, postsynaptic and non-synaptic (vicinal) compartments within tomogram dataset (**Figure 1–table 1**), which were classified as follows: 1) Flat/tubular membrane compartments: Flat membrane tubules 12-20 nm wide that twists along the tubule axis by at least 180°. 2) Large spheroidal membrane compartments: Vesicles with a diameter greater than 60 nm. 3) Multivesicular bodies: Membranous compartments containing at least one internal vesicle. 4) Polyhedral vesicles: Membranous compartment composed of flat surfaces related by ≤90° angle. 6) Dense-cored vesicles. 7) Fission/fusion intermediates: hemifusion intermediates, protein-coated membrane invaginations. 8) Clathrin-coated intermediates: invaginations with a protein coat containing pentagonal or hexagonal openings. 9) Mitochondria: double membrane with cristae and electron-dense matrix. 10) Mitochondrial intermediates: mitochondria with budding outer membrane or putative mitochondrial fragments wrapped by two membrane bilayers. 11) Ribosomes: 25-35 nm electron dense particles composed of small and large subunits. 12) F-actin: 7 nm helical filaments. 13) Microtubules: 25 nm filaments. 14) Cargo-loaded microtubules: vesicles attached to

microtubules via 25-30 nm protein tethers.

Molecular density profile analysis

Molecular density analysis (Smith and Langmore, 1992) of the PreSM and PoSM compartments from ultra-fresh synapse and in-tissue cryo-section tomgramss was carried out using voxel intensity line profiles of the presynaptic and postsynaptic membrane measured using IMOD, Fiji, and custom scripts. Only PSD95-GFP-labelled synapse tomograms were analysed and tomograms were only excluded from analysis if they were oriented on the missing wedge, or if ice contamination, EM grid carbon or cutting damage obscured the PoSM cytoplasm (see **Figure 1–figure supplement 3** and **Figure 2–figure supplement 1B** showing tomographic slices of each ultra-fresh and in-tissue synapse tomogram, respectively). All profiles were made at central regions of each synapse, containing docked presynaptic vesicles and clusters of ionotropic glutamate receptors (**Figure 1–figure supplement 3**), because this is where the PSD is consistently located in synapses imaged by conventional EM. Line profiles (36 nm wide and 450 nm long) from 31 single tomographic slices from synapses with PoSM and PreSM oriented on the *z*-axis of the tomographic volume were measured. Note, projecting multiple tomographic slices, often used to analyse molecular density of the synapse, will only provide accurate profiles of the cytoplasm if the PoSM is perfectly oriented in the *z*-direction of the tomographic volume. Inspecting the line profiles of each tomographic slice showed that the majority tomograms contained synapses that were slightly tilted with respect to the *z*-axis (**Figure 1–figure supplement 2A-B**). We observed that projections of these synapses caused the PoSM membrane to smear resulting in erroneous cytoplasmic profiles that contained molecular density from the membrane itself (**Figure 1–figure supplement 2C**). This highlighted a risk of projecting multiple tomographic slices to measure molecular density within a specific compartment. We therefore avoided directly generating a 2D projection of multiple tomographic slices of each tomographic volume. Instead, to avoid this error, individual profiles of each tomographic slice were aligned to the plasma membrane peak before profiles were averaged to estimate the relative density of molecular crowding within sub-volumes of the PreSM and PoSM compartments of each synapse (**Figure 1–figure supplement 2D**). To ensure molecular

density analysis was capable of detecting a PSD, similar line profiles were taken from samples prepared for conventional EM (see sample preparation details below, **Figure 2H** and **Figure 2–figure supplement 2**) as a positive control.

Quantitative analysis of the PreSM, PoSM, and synaptic cleft

Each membrane was segmented in Dynamo (Castaño-Díez et al., 2017), generating 4,000-20,000 coordinates for each membrane. To refine the contouring of the membrane, subtomograms of the membrane were refined against an average. The synaptic cleft was defined computationally using custom Matlab-based script that identifies the nearest neighbour coordinates between PreSM and PoSM, and vice versa. This gave a dataset of cleft height distances for each synapse, in which more than 99% of measurements were distributed within a range of 10-45 nm and none were greater than 60 nm. The distribution of cleft height distances was plotted using Kernal Density Estimation in Matlab.

Subtomogram averaging

Subtomogram alignment and averaging was performed using Matlab-based scripts derived from the TOM (Nickell et al., 2005) and Av3 (Förster et al., 2005) toolboxes, essentially as previously described (Wan et al., 2017) using initial datasets from only the first 3 mice.

Coordinates of putative ionotropic glutamate receptors were manually picked in UCSF Chimera (Pettersen et al., 2004) using two times binned tomograms with an effective voxel size of 11.94 Å. All membrane proteins with a long-axis extending ~14 nm out of the membrane and an apparent two-fold symmetry axis were picked. The orientation of the normal vector to the membrane surface was determined to define the initial orientation of each subtomogram. The Euler angle defining the final in-plane rotation angle (phi in the av3 annotation) was randomized. The full set of subtomogram positions was split into two independent half sets one for all odd and one for all even subtomogram numbers. The two half sets were processed independently. For initial alignment and averaging, subtomograms with a box size of 64x64x64 voxels (~76.4x76.4x76.4 nm^3)

were extracted from the respective tomograms and averaged. The initial average shows a long, thin stalk. After one iteration of alignment using a low pass filter of 30 Å and a complete in-plane angular search, two-fold symmetry was applied for further iterations. During all steps of alignment and averaging, the missing wedge was modelled as the sum of the amplitude spectra determined from 100 randomly seeded noise positions for each tomogram. After 6 iterations subtomograms with a box size of 96x96x96 voxels (~53.7x53.7x53.7 nm^3) were re-extracted from tomograms with a voxel size of 5.97 Å. Subtomogram positions were reprojected onto the respective tomogram for visual inspection, and mis-aligned subtomogram positions as well as subtomograms that had converged to the same position were removed, reducing the final number of subtomograms to 2368 subtomograms (odd=1182 and even=1186). The two averages were then further refined for 4 iterations using a cylindrical mask tightly fit around the obtained structure and including the membrane and subsequently for 6 more iterations using a cylindrical mask excluding the membrane. To evaluate the final average and assess the resolution obtained, the averages from the two half sets were aligned to each other and the FSC was calculated as described in (*69*) indicating a final resolution of 25 Å (**Figure 4–figure supplement 2A**). The previously reported atomic coordinates of an AMPA subtype ionotropic glutamate receptor (Sobolevsky et al., 2009) (PDB: 3KG2) and NMDA receptor (PDB:5fxh)(Tajima et al., 2016) were fitted as a rigid body into the final subtomogram averaging map using the fit in map tool in UCSF Chimera. The former was a better fit in keeping with the expected higher abundance of AMPA receptors at the synapse (Lowenthal et al., 2015; Spruston et al., 1995).

Cluster analysis

Clustering analysis of glutamate receptors was performed using the DBSCAN algorithm (minimal cluster size 4 and maximal distance between receptors of 70 nm) where the distances between pairs of receptors were defined as the shortest distance between their projections on the surface of the membrane. The mesh associated to the surface was estimated using the "MyOpenCrust" implementation of the crust meshing method and

simplified using the reducepatch from Matlab. The distances between the projected coordinates were computed using the Dijkstra algorithm on the graph associated to the mesh.

We computationally categorised receptor clusters that were situated inside the cleft, in perisynaptic locations outside the cleft, or spanning the boundary of the synaptic cleft. If perisynaptic clusters arose because of detachment of the PoSM and PreSM during sample preparation, we would expect to find at least a small population of PSD95-GFP containing postsynaptic compartments that were not adhered to a pre-synaptic membrane. Examining every single PSD95-GFP puncta in our cryoCLEM dataset of 93 synapses marked a postsynaptic membrane that was also attached to a presynaptic membrane, suggesting synaptic contacts are established in the brain with a high avidity that is not affected by sample preparation.

Supplements

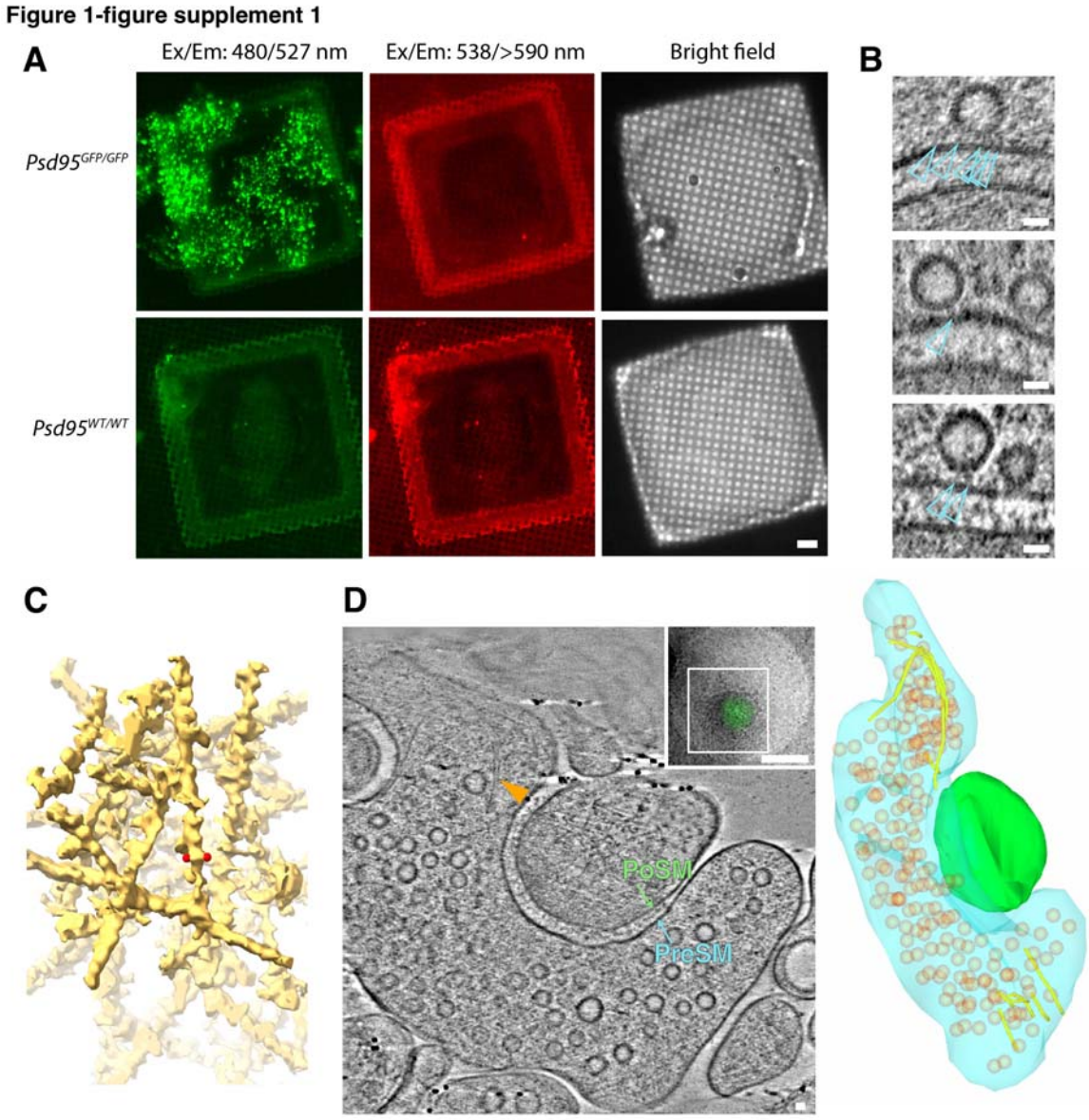

Figure 1–figure supplement 1. CryoFM, docked vesicles and actin in PSD95-GFP-containing synapses.

(A) Cryogenic fluorescence microscopy of forebrain (cortex and hippocampus) ultra-fresh synapse preparation from *Psd95*$^{GFP/GFP}$ (*top panels*) and WT (*bottom panels*). *Left*, detection of GFP with excitation and emission filters of 480 nm and 527 nm, respectively. *Middle*, detection of red fluorescence with excitation and emission filters of 538 nm and >590 nm, respectively.

Right, bright field image. Submicron-sized puncta in the GFP channel only detected exclusively in *Psd95*$^{GFP/GFP}$ samples.

(B) Tomographic slice showing representative docked synaptic vesicles. Docked synaptic vesicles were identified by the macromolecular complexes (open cyan arrow heads) that tethered synaptic vesicles 2-8 nm from the presynaptic membrane. 96% PreSM compartments contained docked synaptic vesicles (see **Figure 1–table 1**). Scale bars, 20 nm.

(C) Masked tomographic map of a branched filamentous actin (F-actin) network in PSD95-containing PoSM compartment. Red spherical markers, spaced 7.1 nm apart on the outside edges of a filament.

(D) Molecular architecture of F-actin in the presynaptic compartment.

Left, tomographic slice through tomogram of synapse located by PSD95-GFP cryoCLEM. F-actin parallel bundle indicated by yellow arrowhead within PreSM (cyan) compartment that was adhered to PoSM (green). See also **Figure 1–video 2**. *Top inset*, PSD95-GFP cryoCLEM image of synapse. White box, indicates White box, indicates region where images for the tomogram were collected. Scale bar, 500 nm.

Right, 3D segmented model of F-actin (yellow tubes) in PreSM (cyan) opposing PoSM (green). Synaptic vesicles (orange). Short F-actin filaments connect a fraction of synaptic vesicles to the plasma membrane. Scale bar, 20 nm.

Figure 1-figure supplement 2

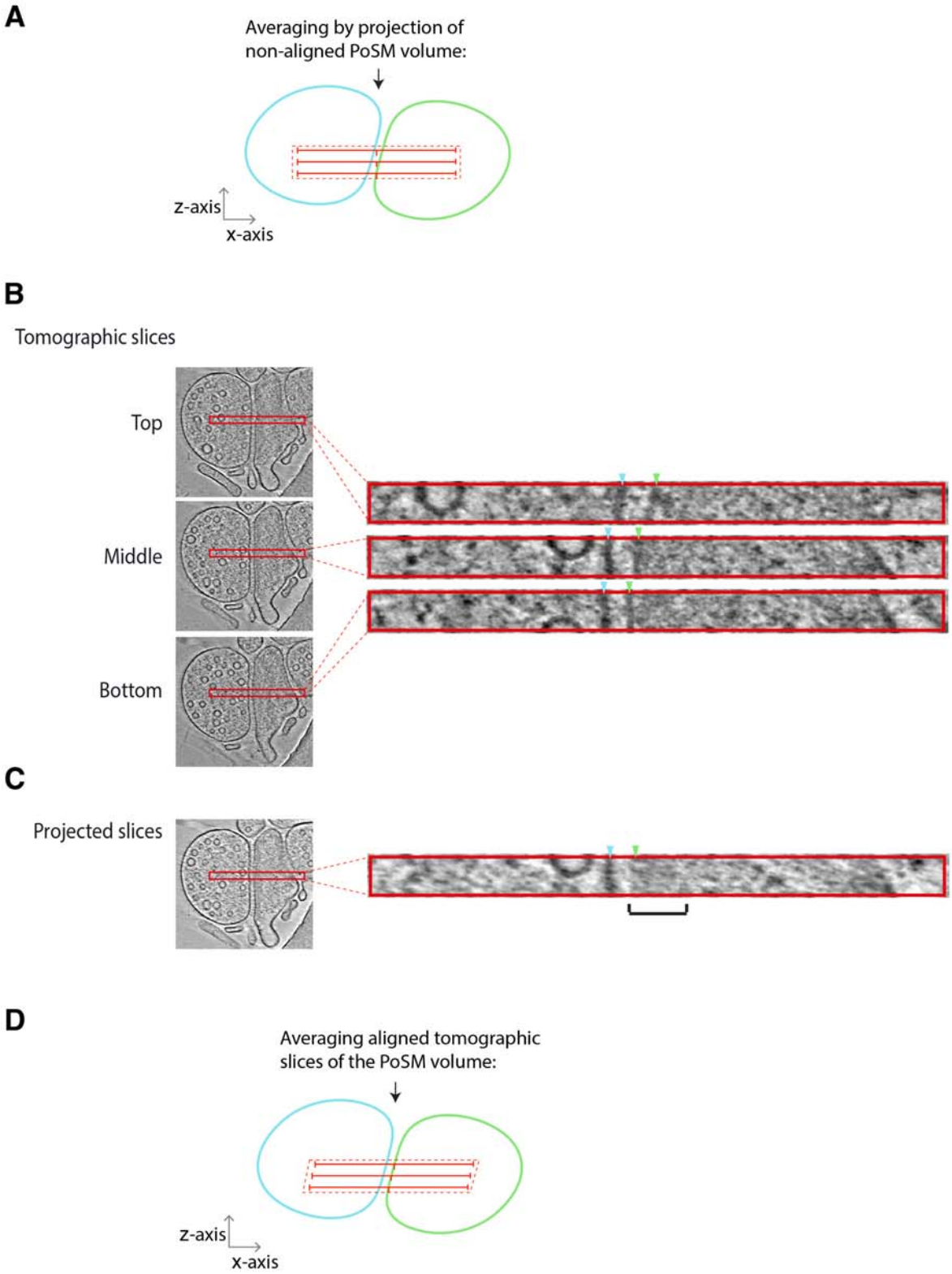

Figure 1–figure supplement 2. Molecular density analysis within synapse tomographic volumes.

(A) Schematic showing an error that arises when projecting a tomographic volume of synapse with a pre- (blue) and post-synaptic (green) compartments that are not perfectly aligned with the *z*-axis of the tomogram. Molecular crowding has been previously analysed using a projection (hatched red rectangle) of multiple tomographic slices (red lines). Projection of such an unaligned volume generates an erroneous molecular density profile in which the plasma membrane and extracellular proteins contribute to measurements of the postsynaptic cytoplasm. Black arrow, direction of the missing wedge.

(B) Example of synapse tomographic volume with postsynaptic membrane not perfectly oriented with z-axis. *Left* and *right*, tomographic slices sub-volume (red rectangle) of top, middle and bottom of tomographic sub-volume, respectively. Blue and green arrowheads, position of PoSM and PreSM in each tomographic slice of the sub-volume, respectively. Note, the position of the PoSM changes in different slices of the sub-volume.

(C) Projection of unaligned tomographic slices with black bracket showing error caused by regions of molecular density from the membrane and synaptic cleft smeared into the postsynaptic cytoplasm

(D) Schematic showing how accurate measurements of molecular density of the postsynaptic cytoplasm within a tomographic sub-volume were obtained (**Figure 1G-H** and **2E-F**). To measure molecular density profiles of each tomographic slice were aligned to the PoSM before averaging. Tomographic slices in which the PoSM was tilted in the x-y plane (see top tomographic slice in panel B) were also excluded from the profile.

Figure 1-figure supplement 3

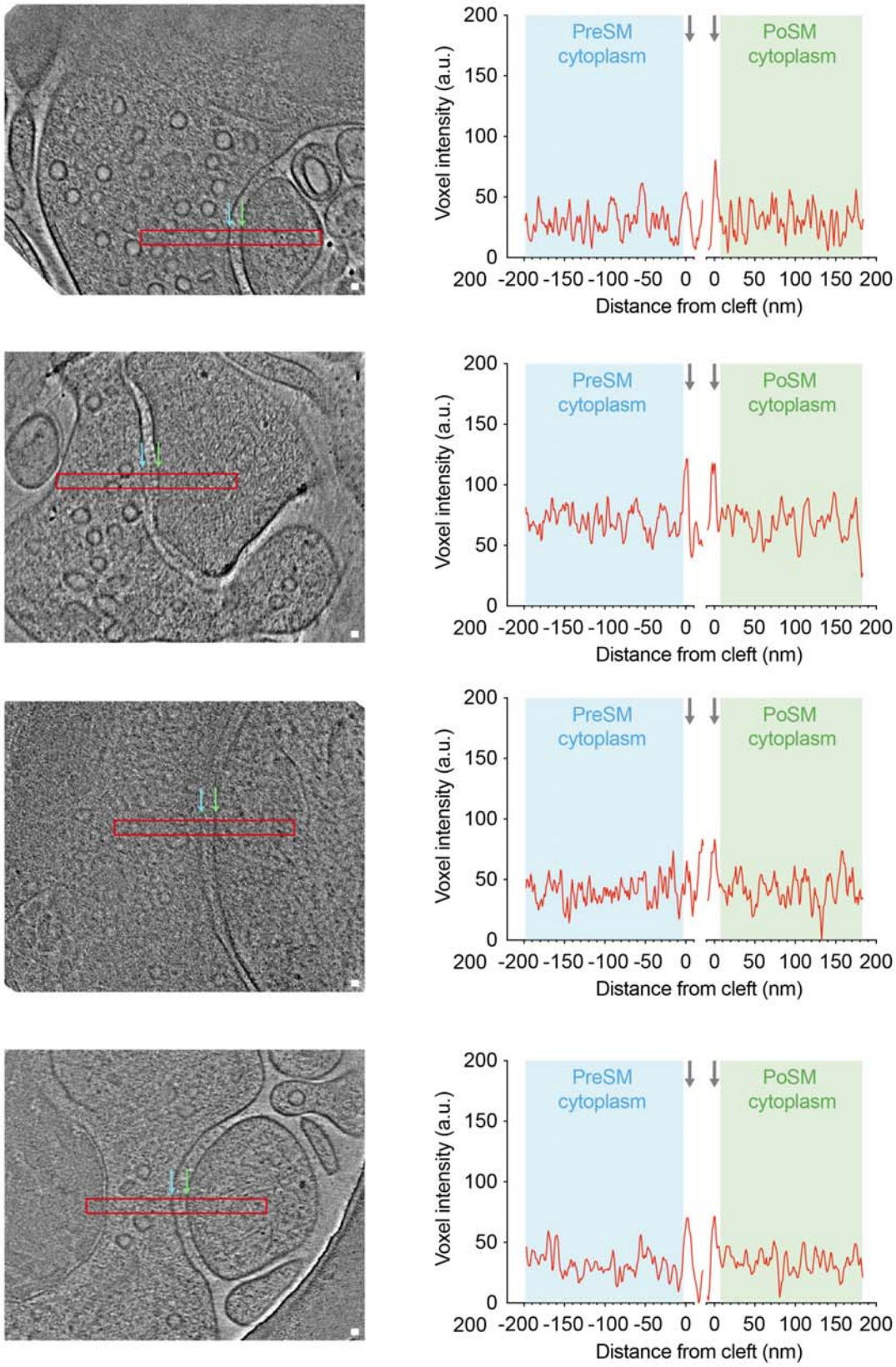

Figure 1-figure supplement 3 cont.

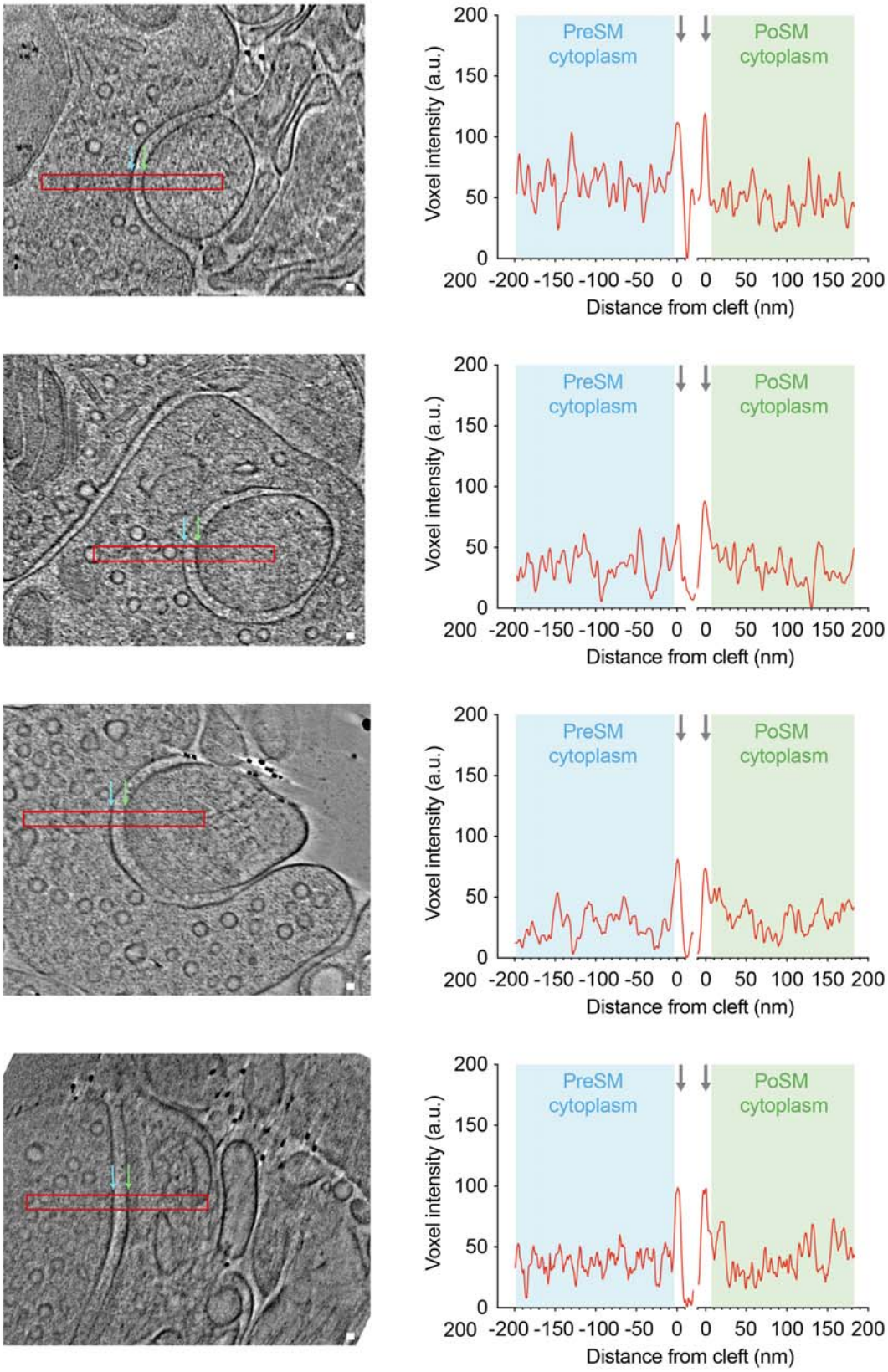

Figure 1-figure supplement 3 cont.

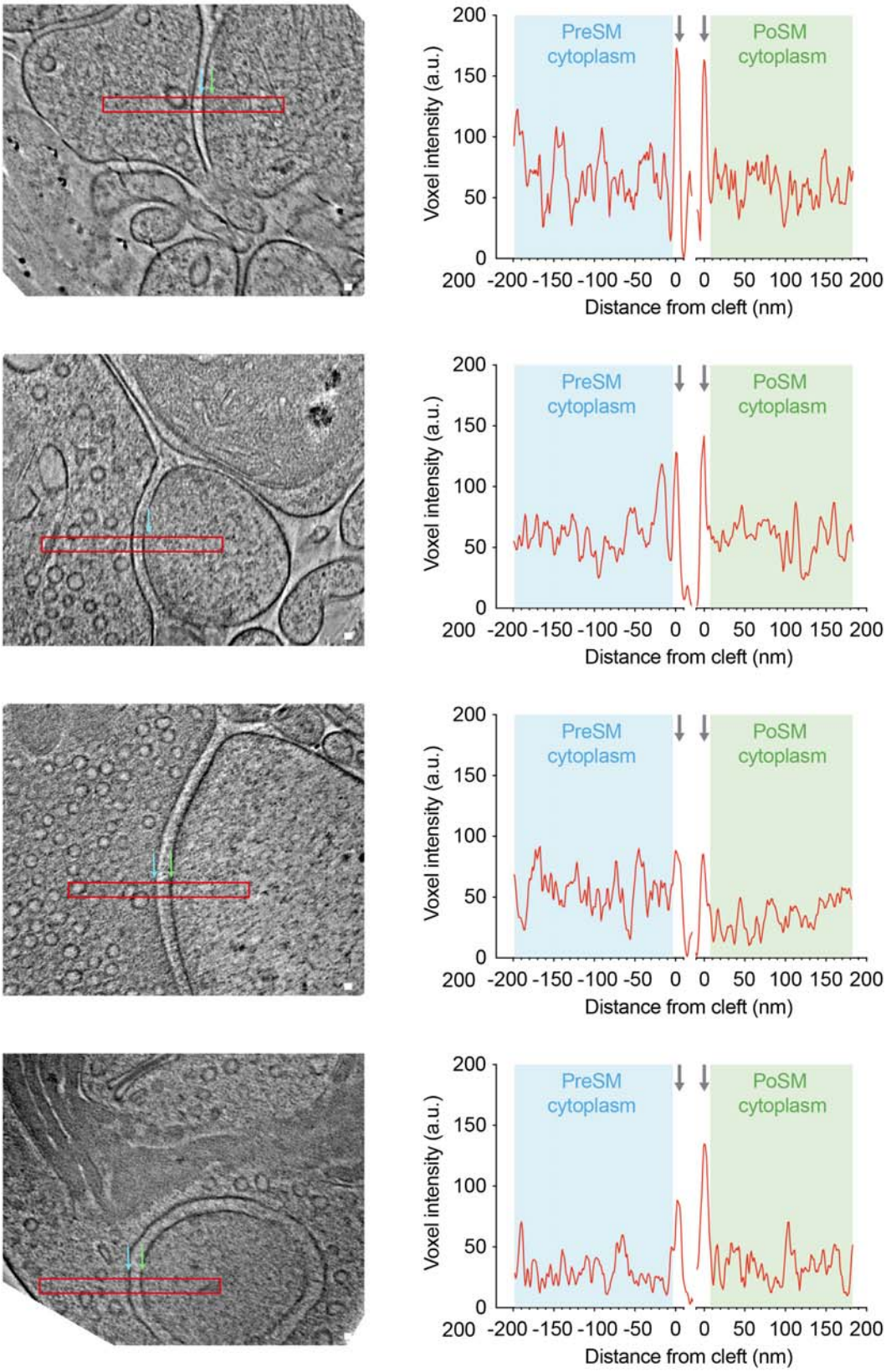

Figure 1-figure supplement 3 cont.

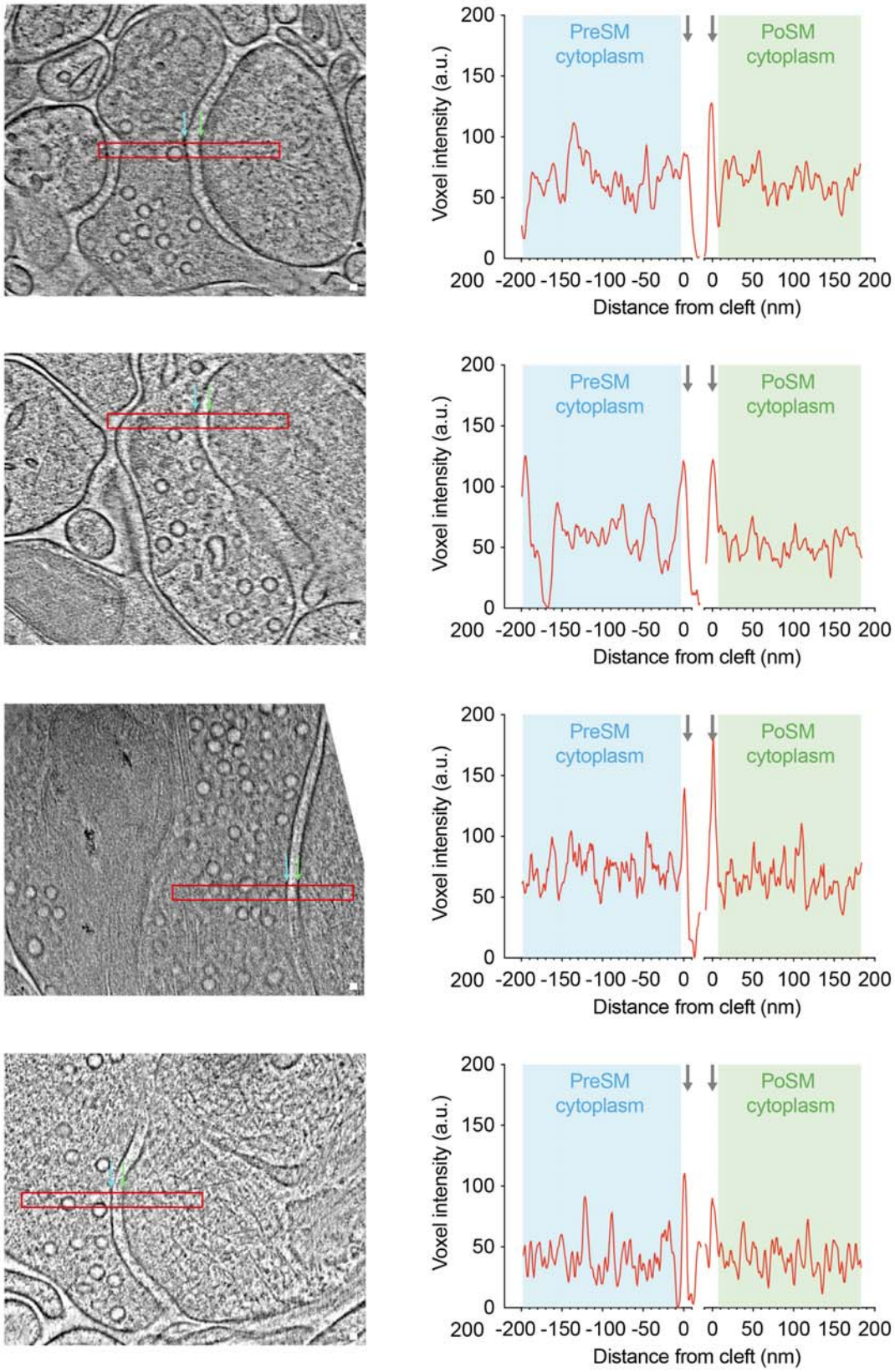

Figure 1-figure supplement 3 cont.

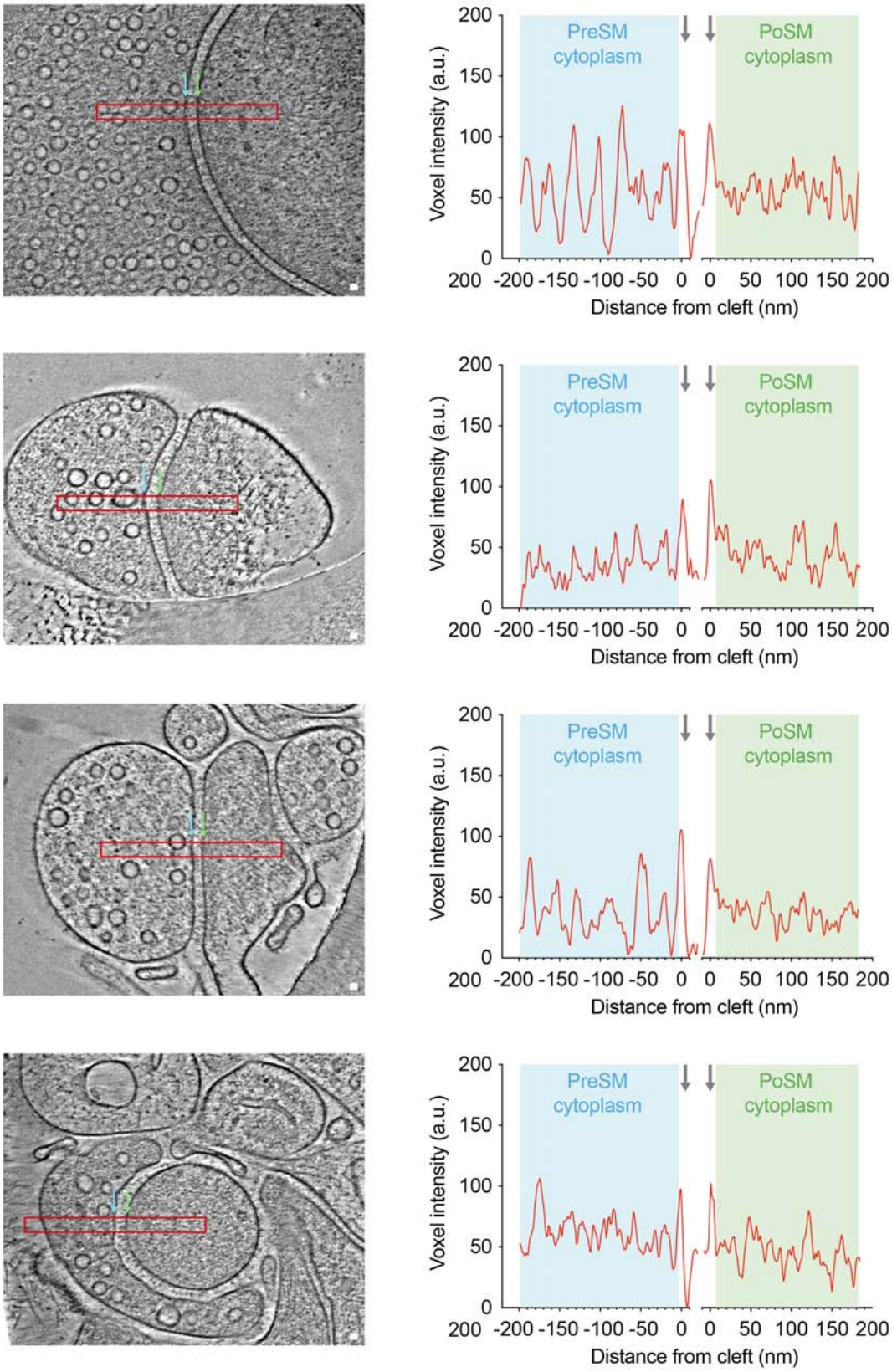

Figure 1-figure supplement 3 cont.

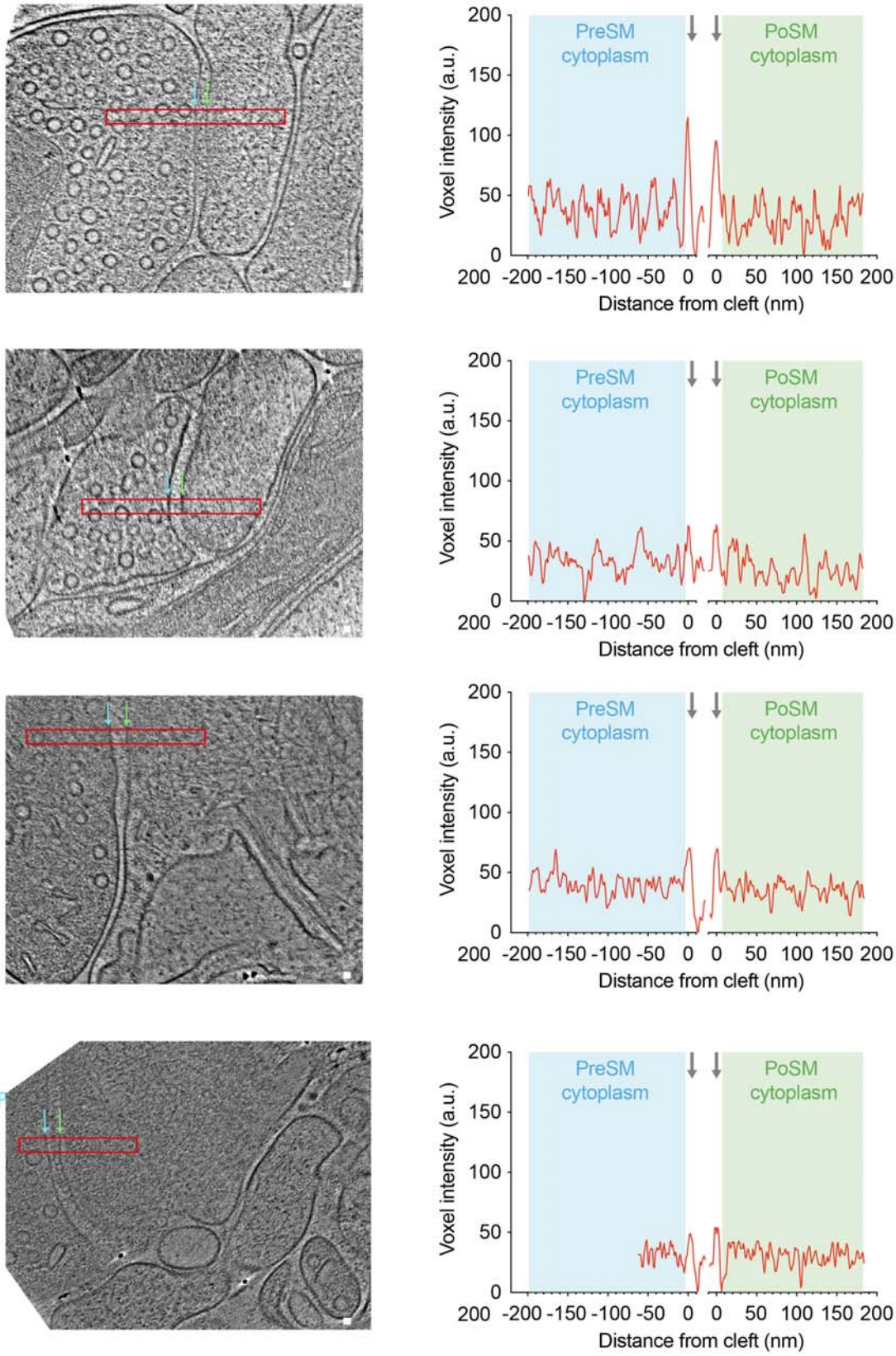

Figure 1-figure supplement 3 cont.

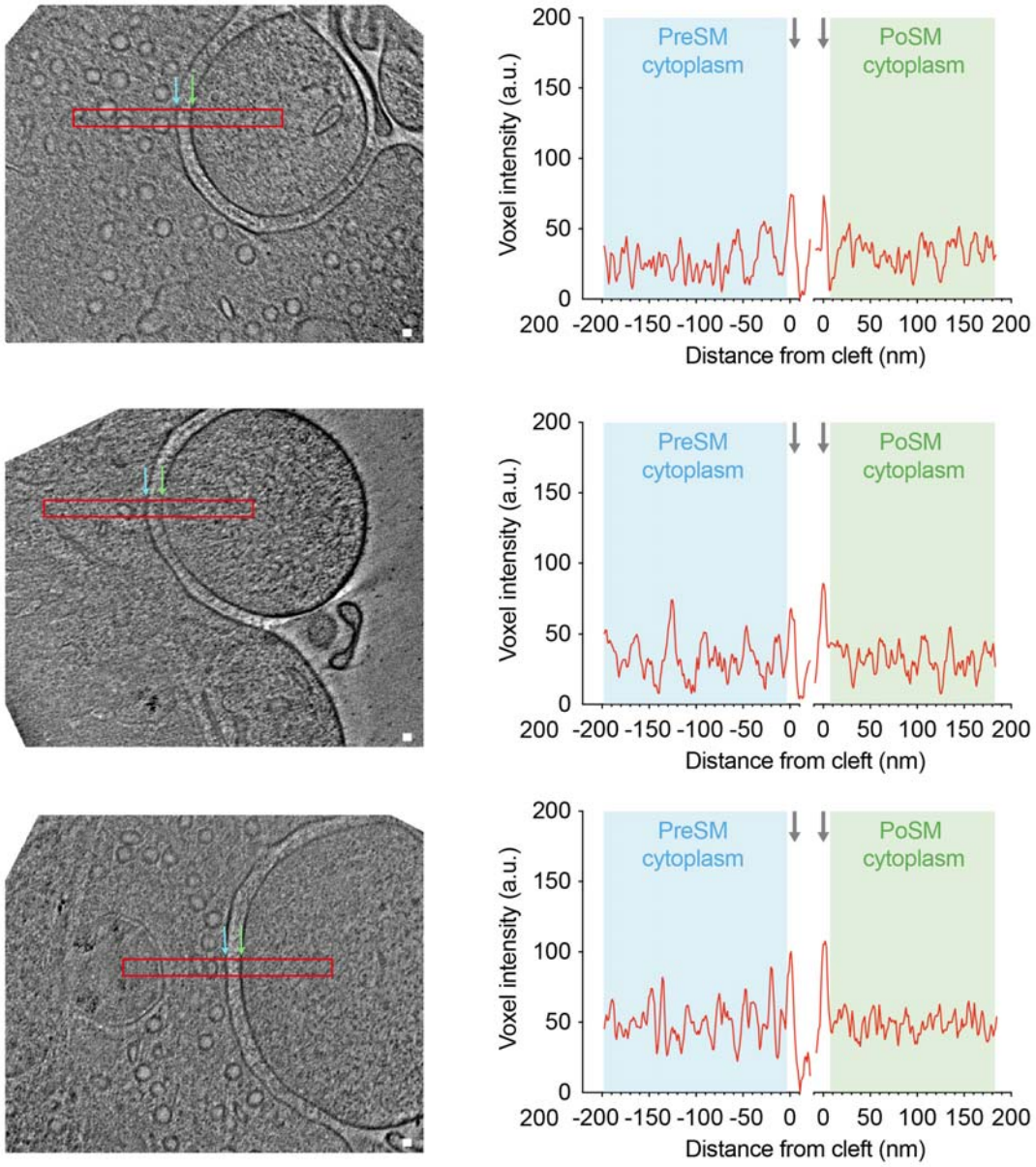

Figure 1–figure supplement 3. Tomographic slices and molecular density profiles of 27 ultra-fresh PSD95-GFP synapses. All tomograms within the ultra-fresh synapse dataset are shown in which the synaptic cleft is approximately parallel to the beam (PreSM and PoSM perpendicular to the *x-y* plane to enable accurate profile measurements of molecular density), and PoSM and PreSM compartments were closed. *Left*, tomographic slice at central regions of synaptic cleft. Red rectangle, region from which profile measuring voxel density were plotted. Scale bar, 20 nm. *Right*, average molecular density profile (36 nm wide and 450 nm long) was measured at central region of the cleft, close to docked synaptic vesicles and clusters of putative ionotropic glutamate receptors, because this is where one would expect to identify a postsynaptic density. Profiles were

aligned to the lipid membrane peak of the PreSM and PoSM (grey arrows). Voxel intensity (a.u., arbitrary units) profile plot of presynaptic (cyan) and postsynaptic (green) cytoplasm. Profiles show that the appearance of high molecular density corresponding to a PSD is not conserved in these samples compared to synapse imaged by conventional EM (see **Figure 2G-H** and **Figure 2–figure supplement 2**).

Figure 2-figure supplement 1

A

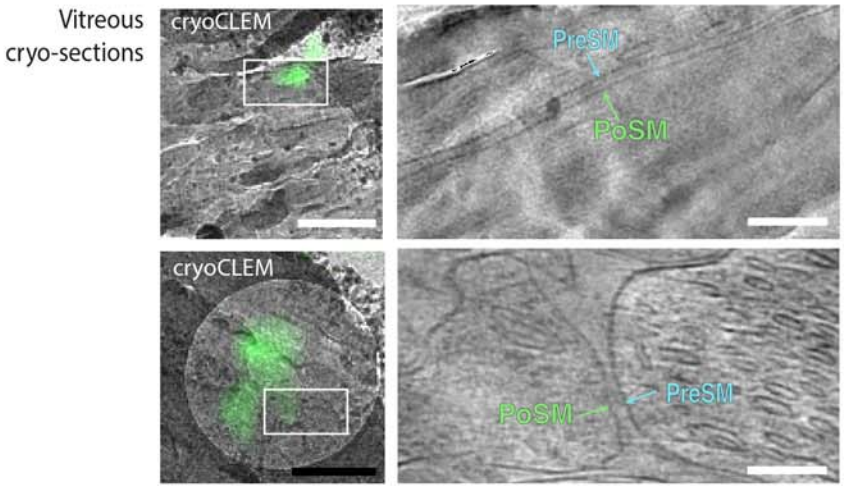

B

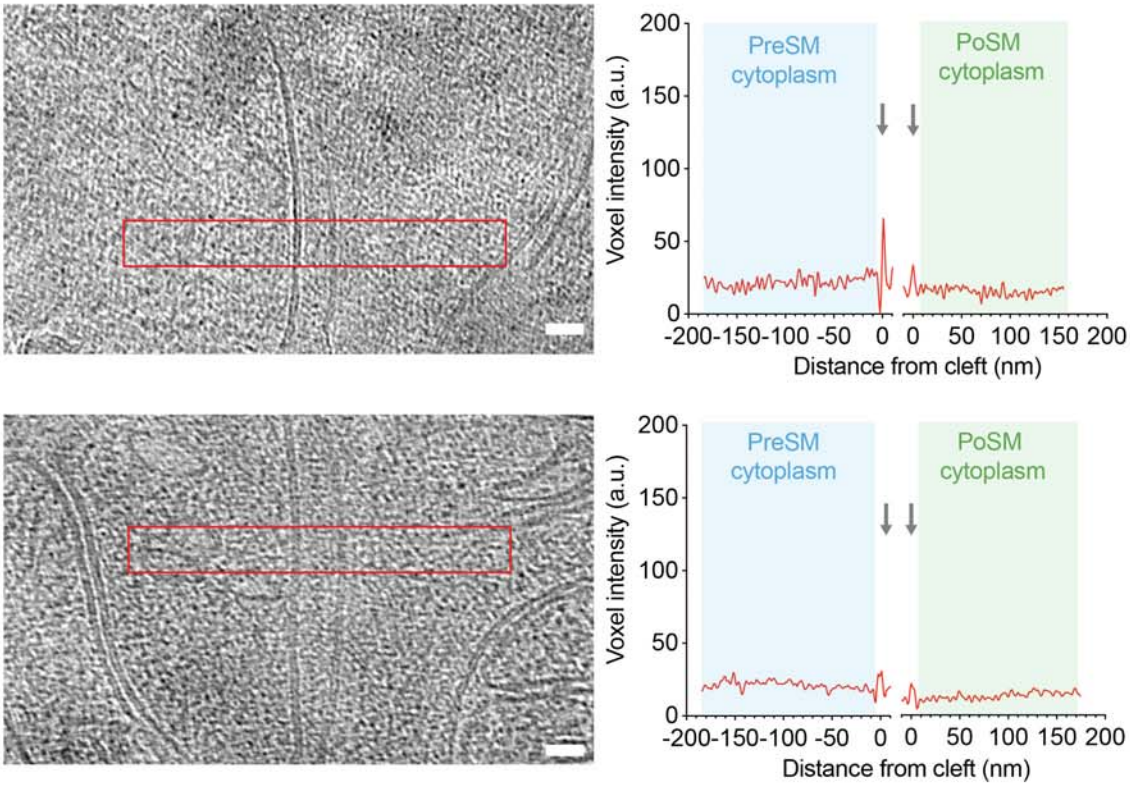

Figure 2-figure supplement 1 cont.

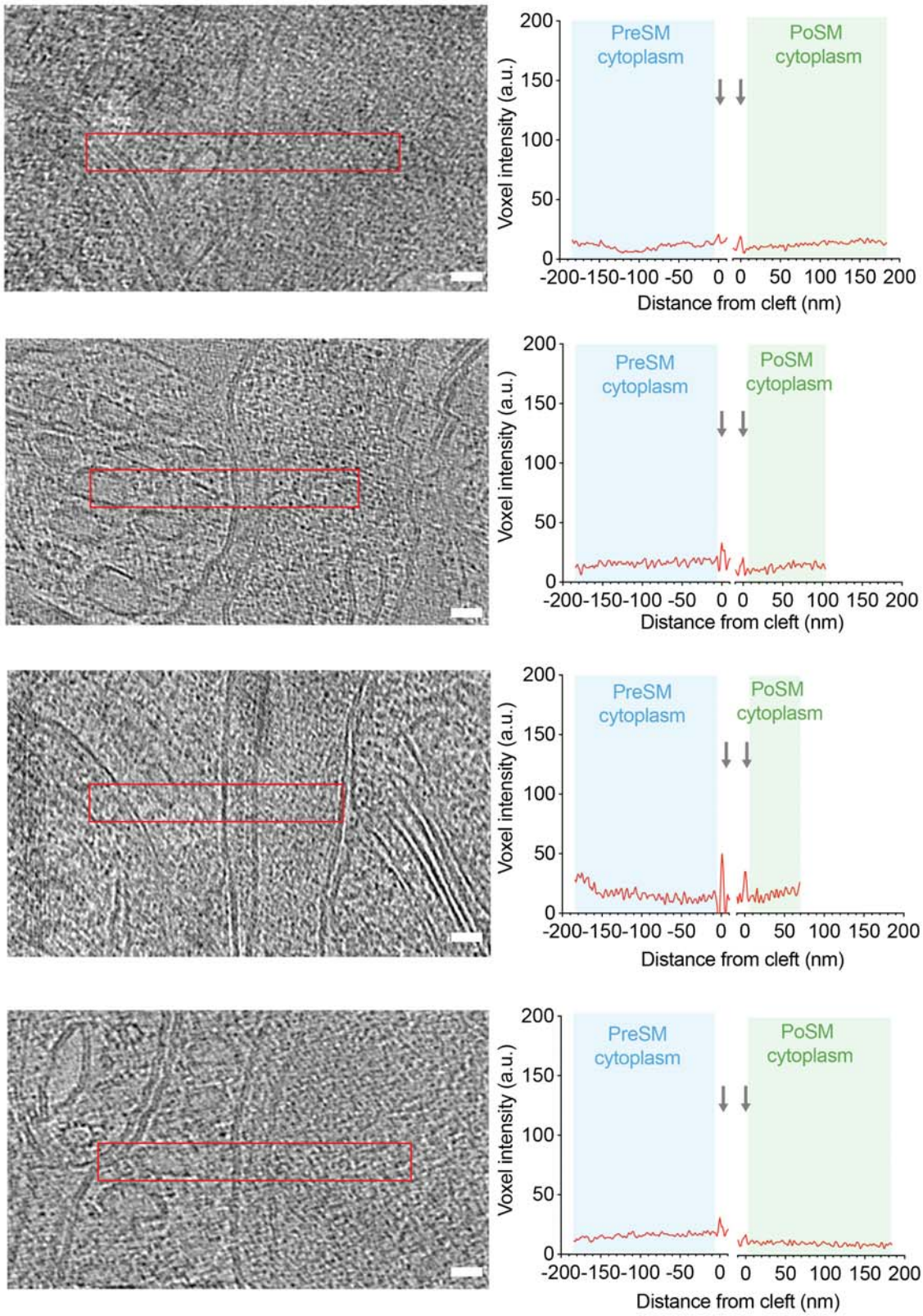

Figure 2-figure supplement 1 cont.

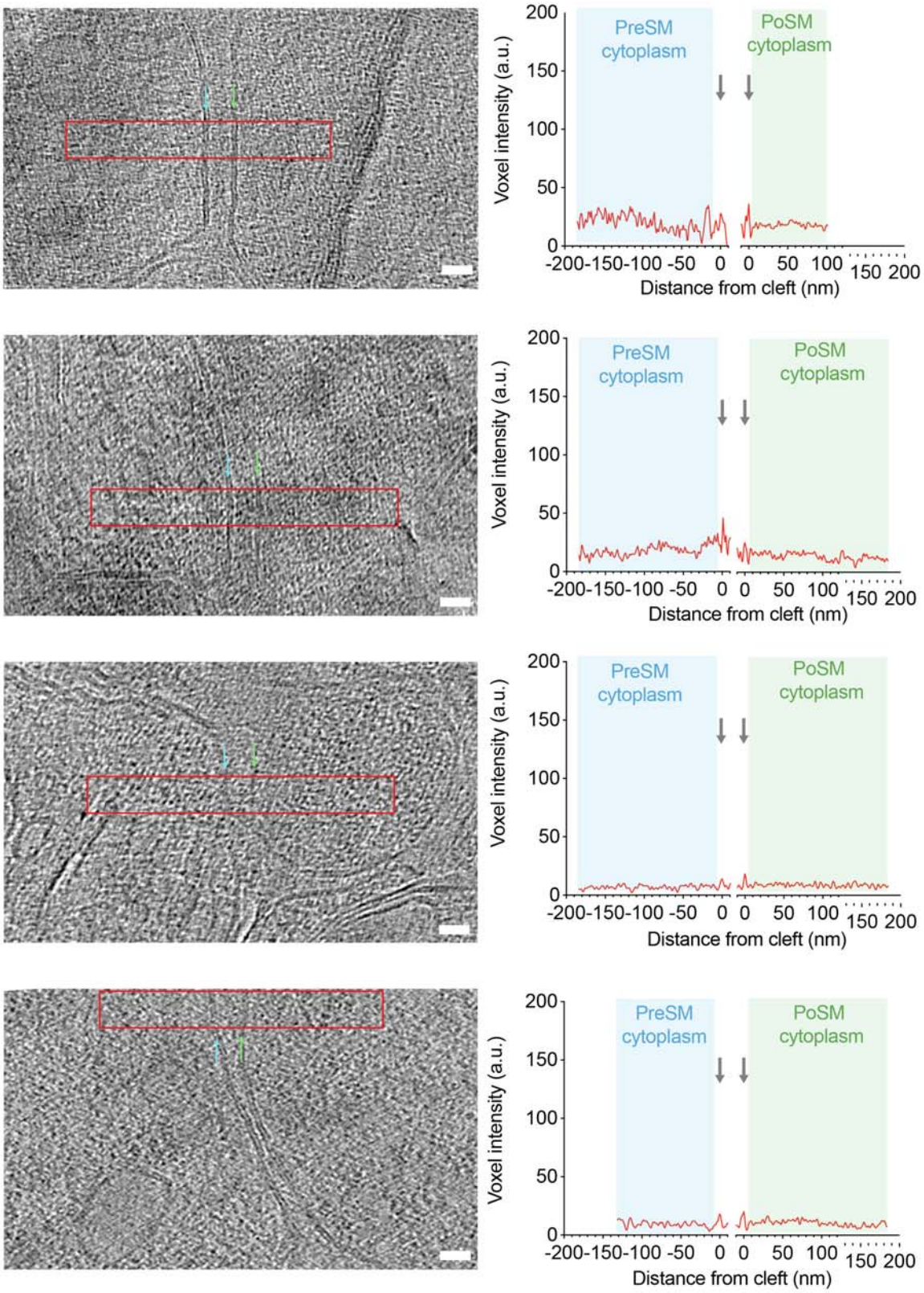

Figure 2-figure supplement 1 cont.

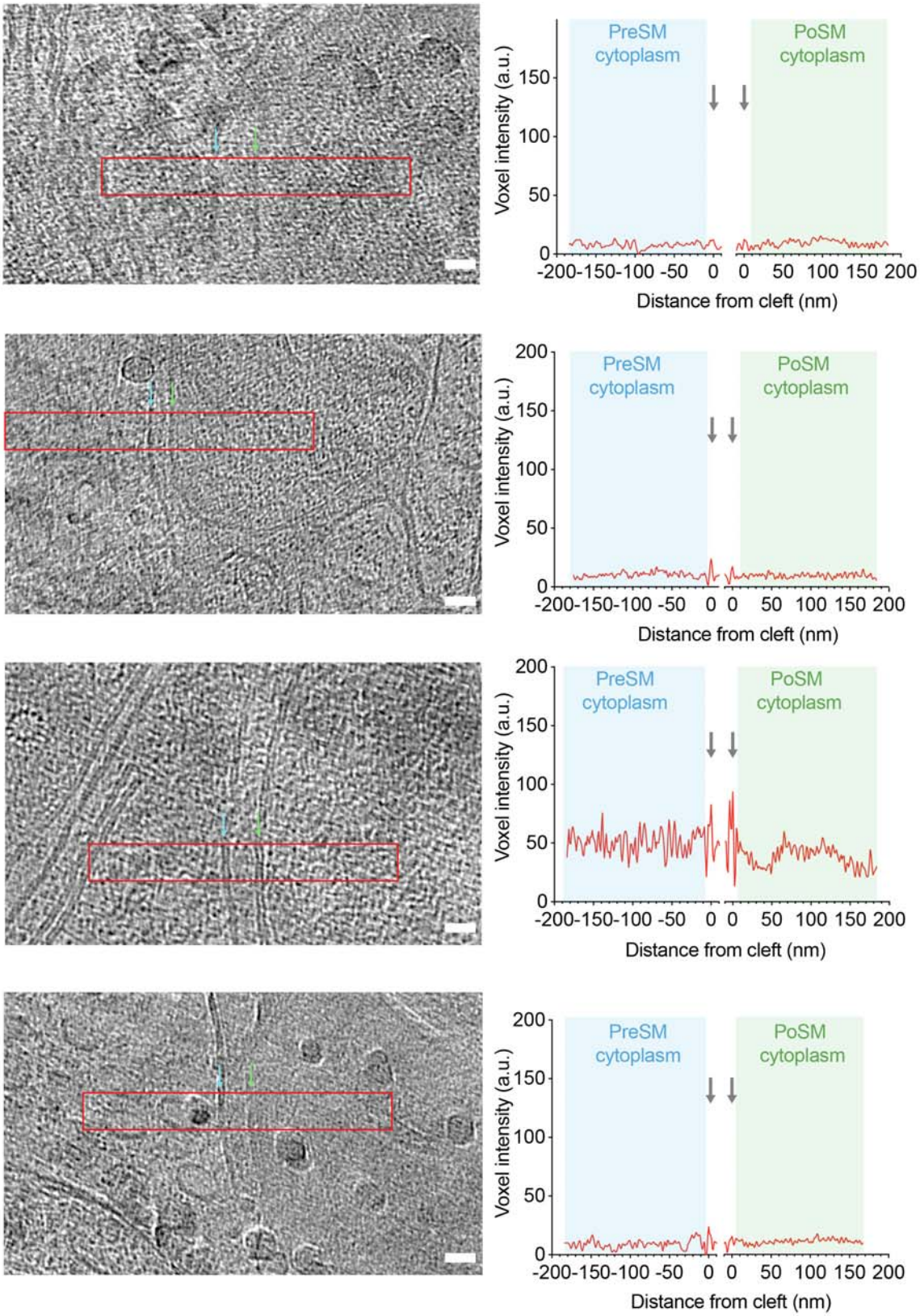

Figure 2-figure supplement 1 cont.

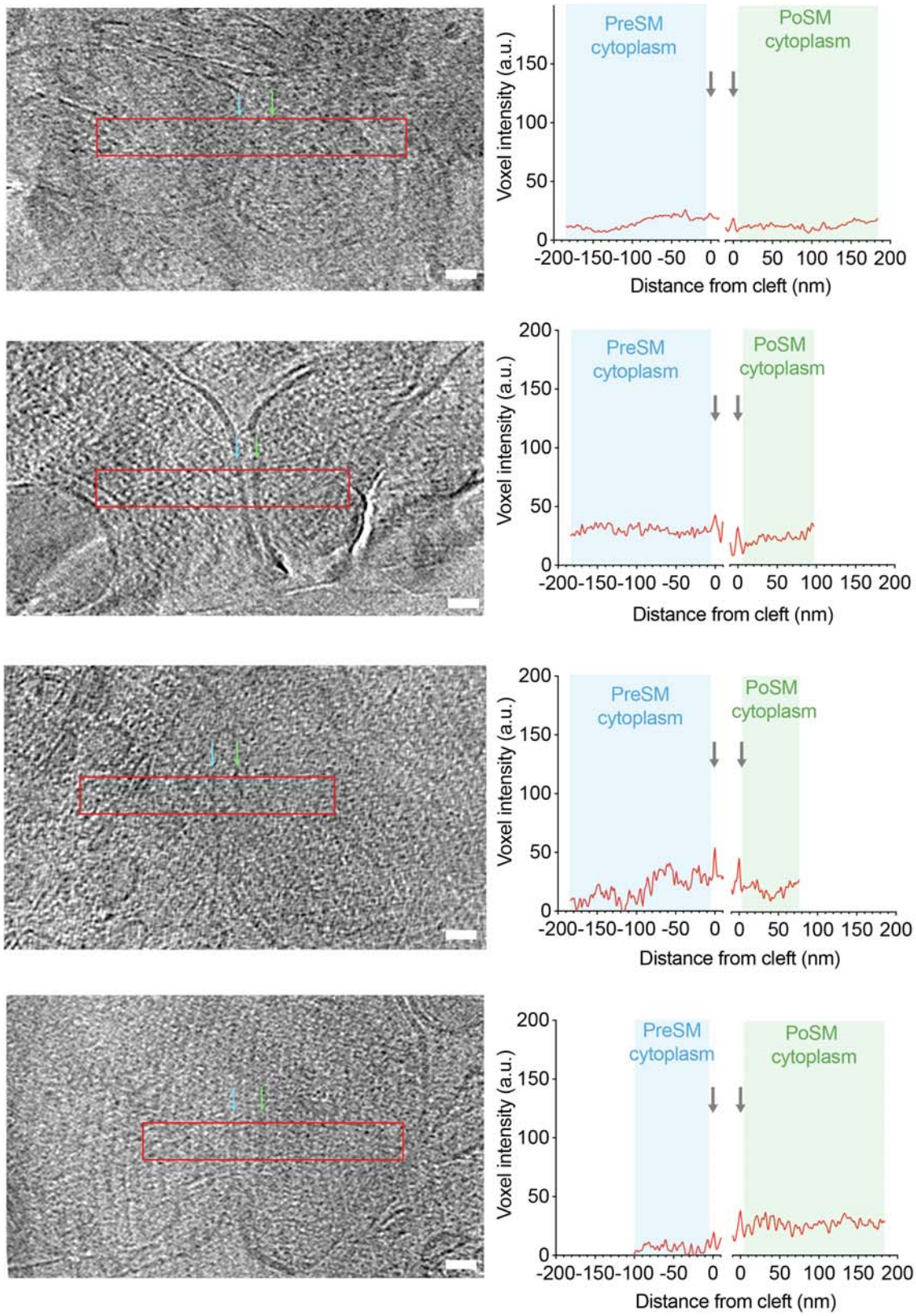

Figure 2-figure supplement 1 cont.

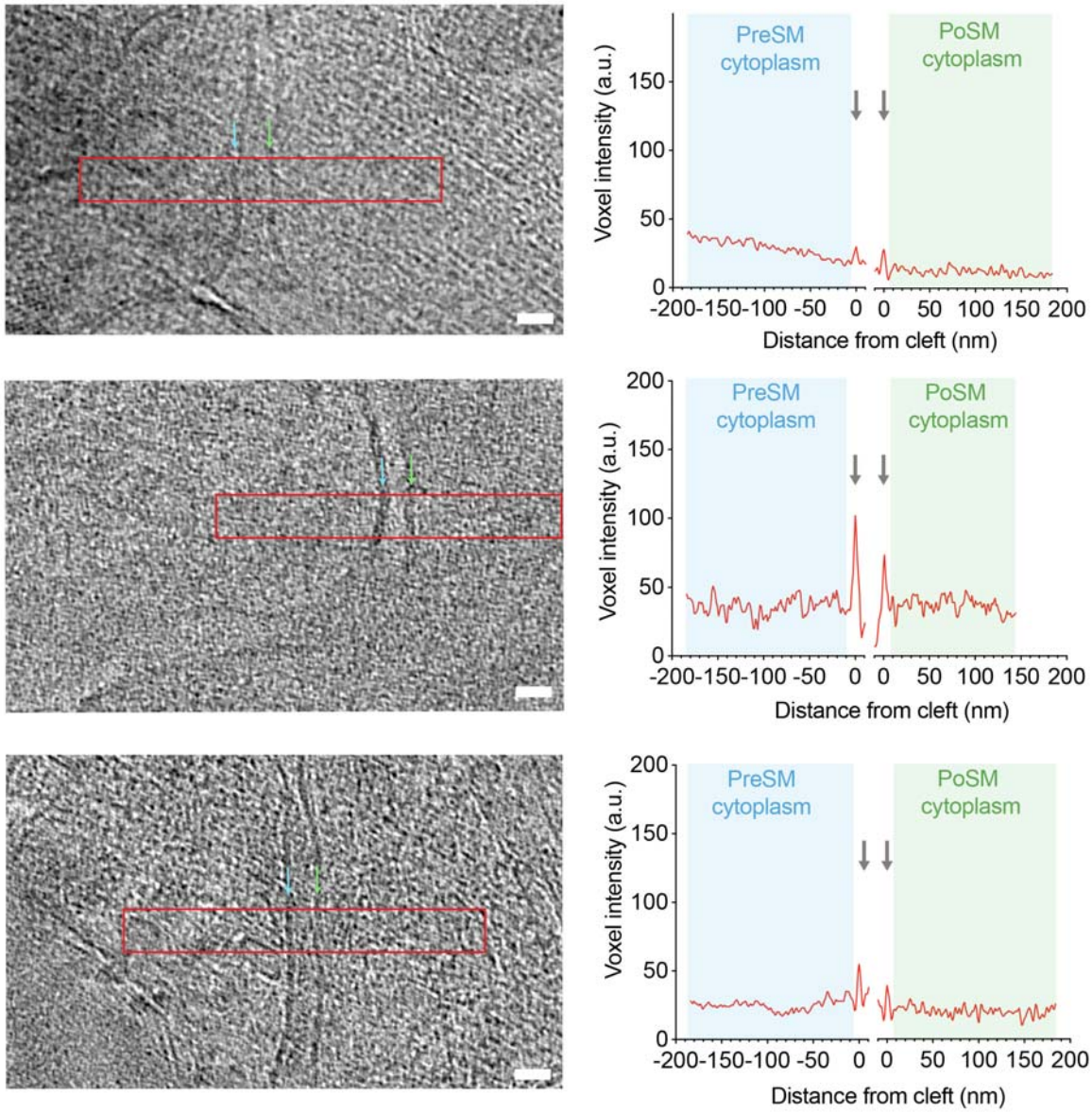

Figure 2–figure supplement 1. Molecular density profiling and tomographic slices of 21 in-tissue cryosection tomograms containing PSD95-GFP synapses.

(a) CryoCLEM and cryoET of two synapses in vitreous cryo-sections collected from adult *Psd95*$^{GFP/GFP}$ knockin mouse cortex. *Left,* PSD95-GFP cryoCLEM image of in-tissue synapse. Scale bar, 500 nm. White box, field of view in *right*, tomographic slice of PSD95-GFP containing synapse within thin vitreous cryo-section of adult mouse cortex. Cyan, PreSM. Green, PoSM. Scale bar, 50 nm. See also **Figure 2–video 2**.

(b) Tomographic slices and molecular density profiles of 21 in-tissue PSD95-GFP synapses. All tomograms within the in-tissue synapse dataset are shown in which the synaptic cleft is approximately parallel to the beam (PreSM and PoSM perpendicular to the *x-y* plane to enable accurate profile measurements of molecular). *Left*, tomographic slice at central regions of synaptic cleft. Red rectangle, region from which profile measuring voxel density were plotted. Scale bar, 20 nm. *Right*, Average molecular density profile (36 nm wide and 450 nm long) was measured at central region of the cleft, close to docked synaptic vesicles and clusters of putative ionotropic glutamate receptors, because this is where one would expect to identify a postsynaptic density. Profiles corresponding to a 37 nm sub-volume were aligned to the lipid membrane peak of the PreSM and PoSM (grey arrows). Voxel intensity (a.u., arbitrary units) profile plot of presynaptic (cyan) and postsynaptic (green) cytoplasm. Profiles show that the appearance of high molecular density corresponding to a PSD is absent in these samples compared to synapse imaged by conventional EM (see **Figure 2G-H** and **Figure 2–figure supplement 2**).

Figure 2-figure supplement 2

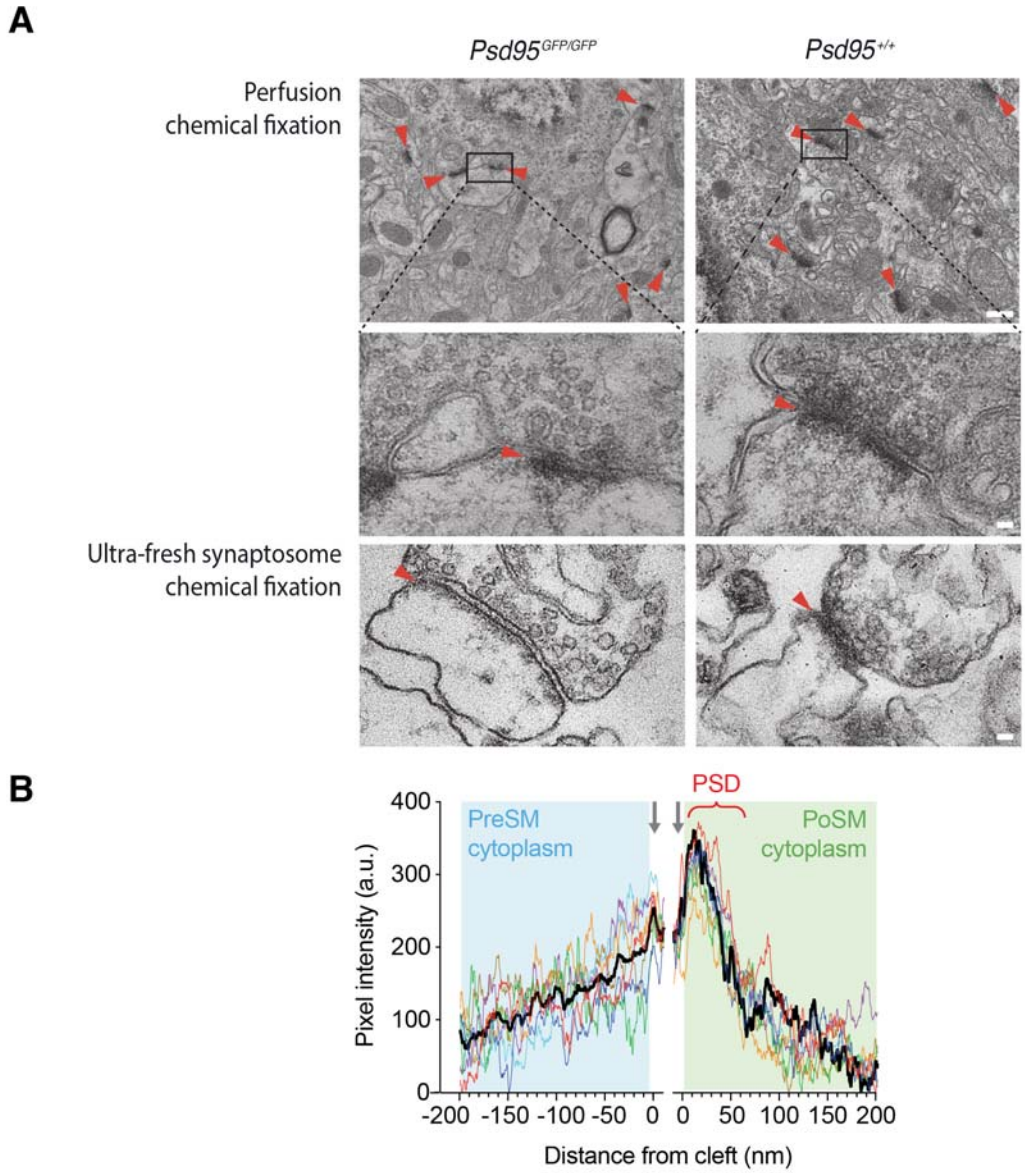

Figure 2–figure supplement 2. Conventional EM of adult brain glutamatergic synapses.

(A) Conventional EM of synapses in, resin-embedded, heavy metal-stained *Psd95*$^{GFP/GFP}$ knockin (left) and wildtype (right) mouse. Red arrowhead, postsynaptic density. Scale bar, 50 nm. *Top*, Electron micrograph showing multiple post-synaptic densities (PSDs, red arrowheads) from perfusion fixed cortex. Scale bar, 500 nm. Black box, PSD shown in *middle* close up. *Bottom*, Conventional EM of ultra-fresh forebrain synapses chemically fixed for conventional EM. Scale bar, 50 nm.

(B) Molecular crowding of the PreSM and PoSM cytoplasm of perfusion fixed *Psd95*$^{GFP/GFP}$ knockin mouse cortex. Pixel intensity (a.u., arbitrary units) profile plots of presynaptic (cyan) and postsynaptic (green) cytoplasm. Profiles were aligned to the lipid membrane peak of the PreSM and PoSM (grey arrows). The average intensity profile of 9 synapse tomograms is shown in black. PSD, postsynaptic density.

Figure 3-figure supplement 1

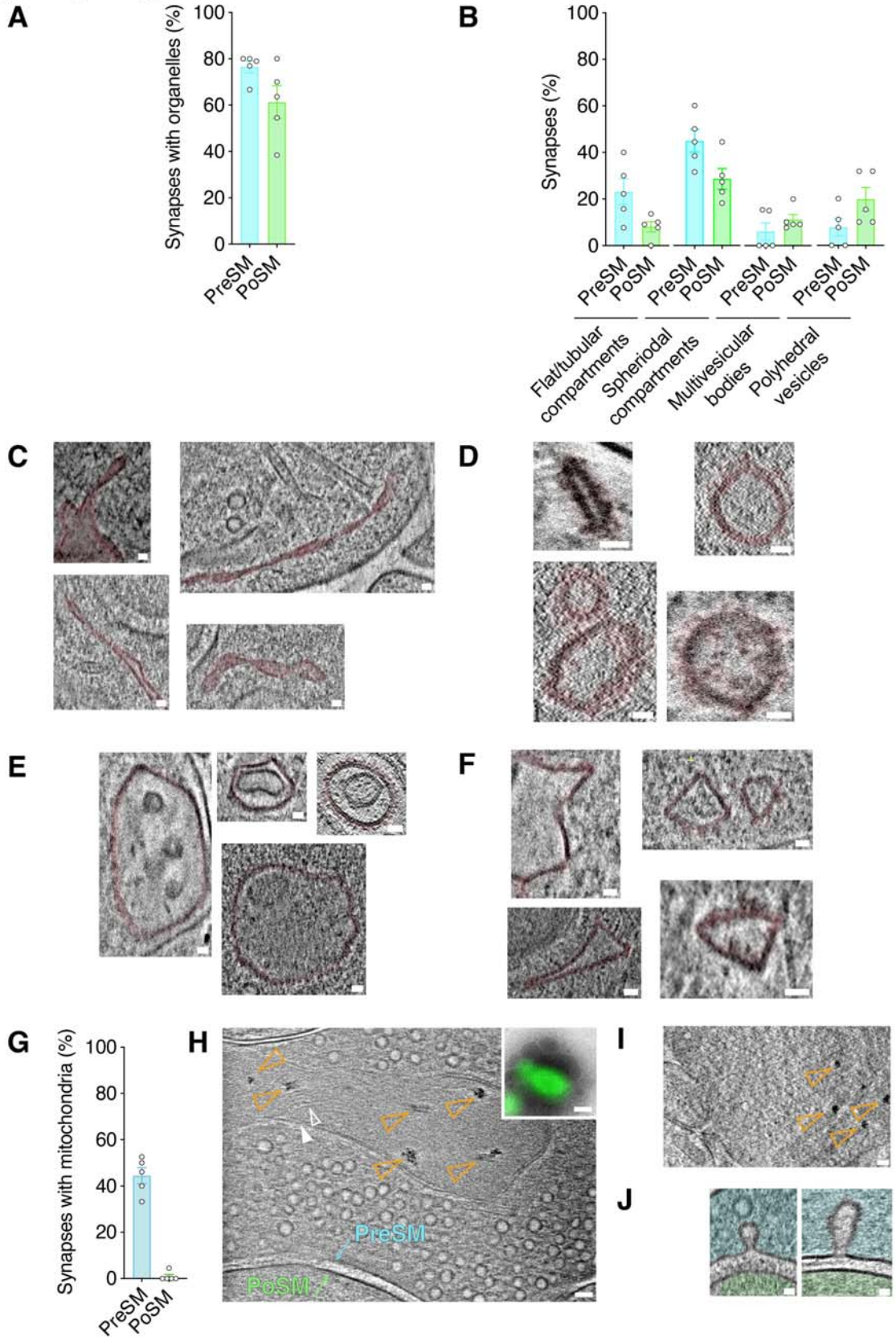

Figure 3–figure supplement 1. Structural categories of membrane-bound organelles in PSD95-containing synapses in the adult brain.

(A) Prevalence of membrane bound organelles within the PreSM (cyan) and PoSM (green) compartments identified in tomograms of forebrain PSD95-GFP containing synapses from 5 adult *Psd95*$^{GFP/GFP}$ mice. Error bars, SEM.

(B) Prevalence of structural classes of membrane-bound organelles, including polyhedral vesicles, flat/tubular membrane compartments, large spheroidal membrane compartments (>60 nm diameter), multivesicular bodies, and polyhedral vesicles within the PreSM (cyan) and PoSM (green) compartments of PSD95-containing forebrain synapses from 5 adult *Psd95*$^{GFP/GFP}$ mice. Error bars, SEM.

(C-F) Classification of membrane-bound organelles in PSD95-GFP-containing synapses. Gallery of tomographic slices showing intracellular organelle subtype (pseudo-coloured magenta) of four different PSD95-GFP containing synapses of

(C) Flat tubular twisted membranes.

(D) Clustered membrane proteins in vesicles.

(E) Multivesicular bodies.

(F) Polyhedral membranes.

Scale bar, 20 nm

(G-I) Synaptic mitochondria.

(G) Bar chart showing the prevalence of mitochondria in the pre- (PreSM) and post-synaptic membrane (PoSM) compartments of glutamatergic synapses.

(H) Tomographic slice of synapse located by PSD95 cryoCLEM showing PreSM containing mitochondria identifiable by surrounding outer membrane (solid white arrowhead) and inner cristae membrane (open white arrowhead). Electron-dense deposits in the mitochondrial matrix are indicated with open orange arrowheads. Scale bar, 50 nm. *Top inset*, PSD95-GFP cryoCLEM image of synapse. Scale bar, 500 nm.

(I) Same as h, except ultra-fresh synapses (see Methods) were prepared with ACSF omitting calcium chloride. Electron dense deposits within mitochondrial matrix were detected in all (3 out of 3) PreSM compartments. Scale bar, 50 nm.

(J) Tomographic slices of synapses with intermediates of vesicle fusion/fission on the presynaptic side of the cleft of a PSD95-GFP containing synapse. *Left*, small intermediate. *Right*, Large intermediate. Scale bar, 20 nm.

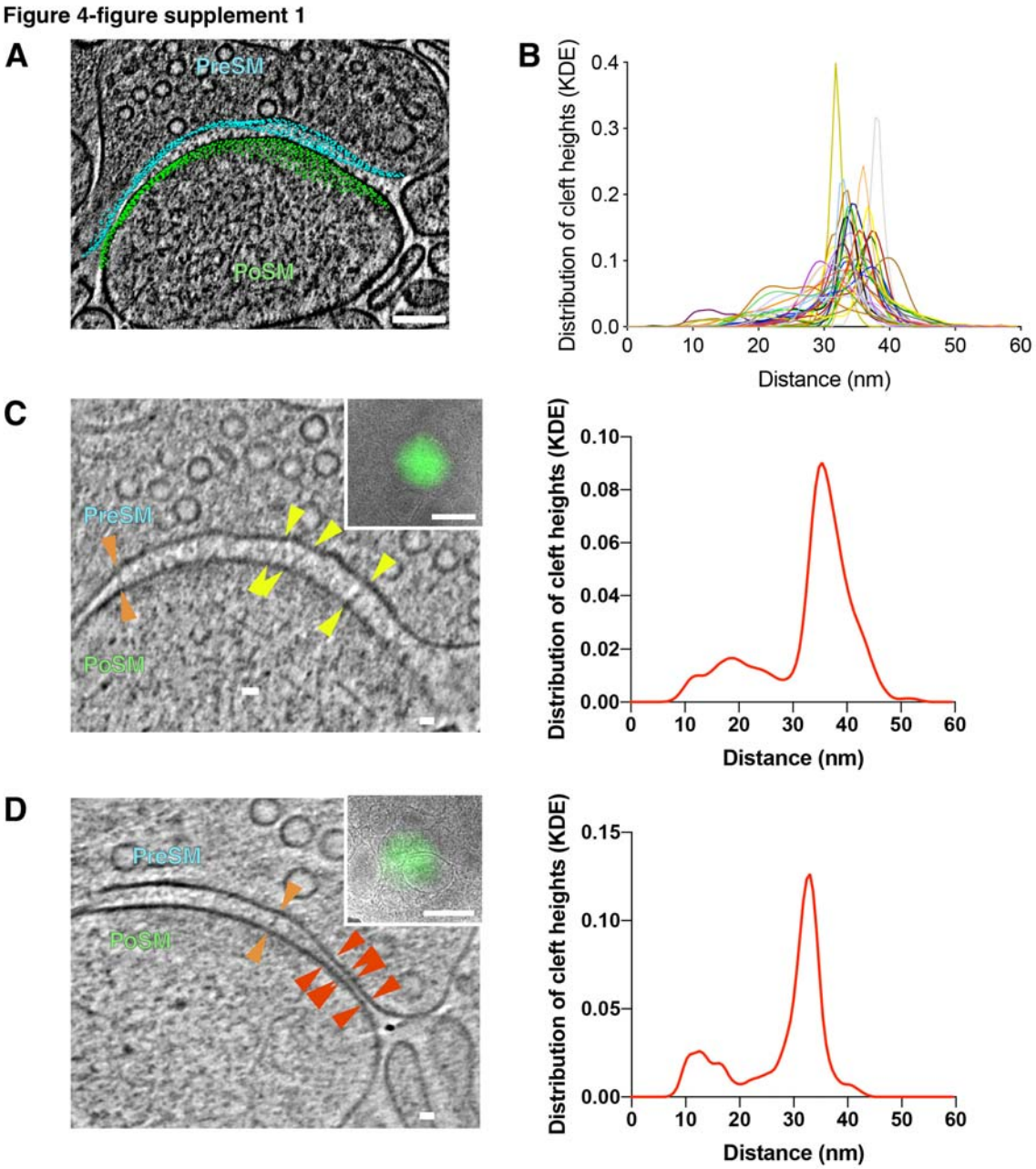

Figure 4–figure supplement 1. Quantification and variability of cleft height in glutamatergic synapses.

(A) Tomographic slice of PSD95-GFP containing synapse. 3D model of computationally determined coordinates of synaptic cleft are shown with presynaptic and postsynaptic cleft membrane coordinates depicted in cyan and green, respectively. Scale bar, 100 nm.

(B) Measuring the nearest neighbour distance between presynaptic and postsynaptic coordinates of the cleft were used to quantify the cleft heights for each synapse. The distribution of cleft

height distances is shown using kernel density estimation (KDE) plotted with a different colour for each synapse.

(C and D) Synapses with a bimodal distribution of cleft hights. *Left*, tomographic slice of PSD95-GFP containing synapses showing subsynaptic regions with varying cleft height between PreSM (cyan) and PoSM (green). Red arrowheads, 5-15 nm transsynaptic adhesion complexes. Orange arrowheads, 22-28 nm transsynaptic adhesion complexes. Yellow arrowheads, 32-36 nm transsynaptic adhesion complexes. Scale bar, 20 nm. *Top inset*, PSD95-GFP cryoCLEM image of synapse. Scale bar, 500 nm. *Right*, the corresponding distribution of cleft height distance for each synapse is plotted using kernel density estimation (KDE).

Figure 4-figure supplement 2

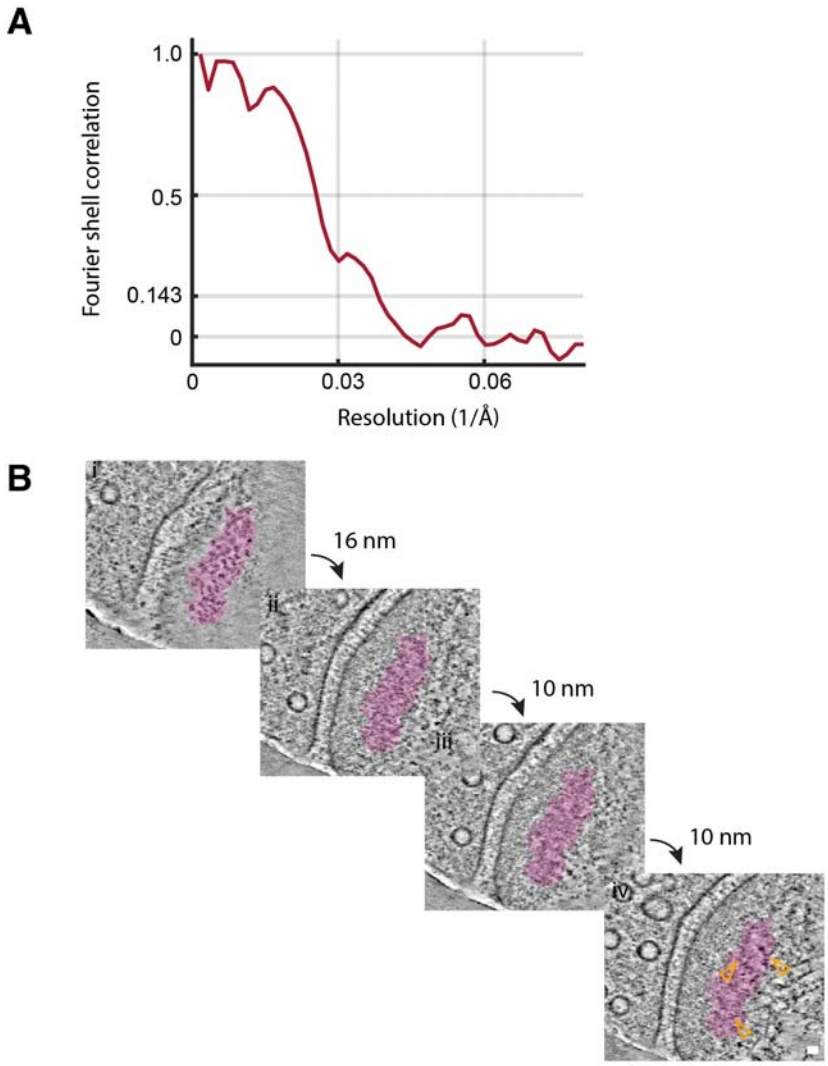

Figure 4–figure supplement 2. Subtomogram averaging and anchoring of ionotropic glutamate receptors.

(A) Estimation of the resolution of subtomogram averaged ionotropic glutamate receptors shown by plotting with a linear scale the resolution (*x*-axis) versus global Fourier shell correlation (*y*-axis).

(B) Cytoplasmic anchoring of perisynaptic ionotropic glutamate receptor clusters (pseudo-coloured in magenta). Cluster was defined using DBSCAN. Tomographic slices through tomogram of PSD95-GFP containing postsynaptic compartment. Slices separated by 16, 10, 10 and 10 nm, showing top-down views of i) extracellular membrane protein domains, ii) proximal

and iii) distal cytoplasmic macromolecular complexes, iv) associated branched f-actin network (orange open arrowhead). Scale bar, 20 nm.